Nano Today 29 (2019) 100796

Contents lists available at ScienceDirect

Nano Today

journal homepage: www.elsevier.com/locate/nanotoday

Review

Hard-template synthesis of three-dimensional interconnected carbon networks: Rational design, hybridization and energy-related applications

Shan Zhu[a], Naiqin Zhao[a,b,c], Jiajun Li[a], Xiaoyang Deng[a], Junwei Sha[a,*], Chunnian He[a,b,c,d,*]

[a] School of Materials Science and Engineering and Tianjin Key Laboratory of Composites and Functional Materials, Tianjin University, Tianjin 300350, China
[b] Collaborative Innovation Center of Chemical Science and Engineering, Tianjin 300350, China
[c] Key Laboratory of Advanced Ceramics and Machining Technology, Ministry of Education, Tianjin 300350, China
[d] Joint School of National University of Singapore and Tianjin University, International Campus of Tianjin University, Binhai New City, Fuzhou 350207, China

ARTICLE INFO

Article history:
Received 2 April 2019
Received in revised form 31 August 2019
Accepted 30 September 2019
Available online 15 November 2019

Keywords:
Three-dimensional carbon network
Hard templates
Composite
Nanomaterials
Energy storage
Energy conversion

ABSTRACT

Three-dimensional interconnected carbon networks (3DCNs) materials have the advantages of large specific surface area, high porosity, and high electronic and ionic conductivity. Especially, 3DCNs can combine with other nanomaterials to achieve the synergistic effect in numerous applications, such as energy storage, catalysis, and structural engineering. For the synthesis of 3DCNs, the hard template strategy is the most popular method due to its efficient and versatile process and controllable production. This paper summarized the recent progress in the approaches to constructing 3DCNs by using hard templates including metals, inorganic non-metals, etc. The composites based on 3DCNs with multi-dimensional reinforcements, such as 0D nanoparticles, 1D nanotubes/nanofibers, and 2D nanosheets are introduced. The applications of these 3DCNs composites towards energy storage and conversion devices are reviewed. Furthermore, the challenges on the hard-templated 3DCNs are discussed based on the current progress.

Contents

* Corresponding authors.
E-mail addresses: shajw@tju.edu.cn (J. Sha), cnhe08@tju.edu.cn (C. He).

https://doi.org/10.1016/j.nantod.2019.100796
1748-0132/

Introduction

Three-dimensional carbon network (3DCN) refers to a kind of carbon materials with 3D conductive structures [1,2], which can be defined as a carbon material with uniform function in three-dimensional direction and connected structure distribution. Compared with 0D, 1D, and 2D carbon nanomaterials, the characteristic of 3DCN is a large specific surface area, high porosity, efficient mass transfer and ease of heteroatom doping [3]. Moreover, 3DCNs can serve as a matrix and combine with other nanomaterials to achieve the synergistic physical and chemical effects in certain applications [4–6]. As a result, 3DCNs and their composites have become promising candidates in many state-of-the-art devices, especially in energy-related fields, such as batteries, supercapacitors and fuel cells [4,7,8].

To synthesize 3DCN-based materials, the most commonly adopted strategy is the template method. Template method, including soft template and hard template, enable the researchers to design the component and structure of templates according to the performance and morphology requirements of the target productions [9–11]. Comparing to soft templates, hard templates have higher stability and better space-confined effect, so it can be used to strictly control the size and morphology of nanomaterials. As a result, numerous hard templates have been developed in order to prepare 3DCNs and their composites [12,13].

Generally, the materials used as hard templates are metal, inorganics and many kinds of mixtures, which can maintain their certain microstructures under treatment processes (e. g. high temperature) [14]. In a typical synthesis process, the nanospace in hard templates will fill with carbonaceous precursors firstly, followed with a carbonization process enabling convert the precursors into carbon [13]. Subsequently, these templates are removed by chemical etching or water washing. Based on this simple and efficient process, the hard templates fully play their potential on considerable flexibility and became the widespread method for synthesizing 3DCN-based materials [15]. Especially, several special applications require high surface area and electron conductivity for ensuring sufficient surface reactions, such as electrochemical processes. Therefore, many reviews on the preparation of carbon materials by templates method have been presented previously [9–12]. Yet, 3DCN related hard templates have their own structural and properties features in the preparation process.

Over the past decades, the researches for synthesizing 3DCNs by hard templates have obtained great achievements. We believe that it is worthwhile to summarize recent progress in the hard-templated 3DCN-based materials and their energy-related applications. In Section “Multi-scale hard template for 3DCNs”, we will introduce several typical hard templates and describe the growth mechanism of 3DCNs based on hard templates. Then, we will review the 3DCN-based composites combined with 0D, 1D and 2D nanomaterials synthesized by using hard-templates in Section “Synthesis of 3DCN composites based on hard-templates”. In Section “Energy Storage Applications of 3DCN composites”, we will introduce the applications of 3DCN-based nanomaterials for batteries, supercapacitors and fuel cells. Furthermore, this review will be summarized in the final section with an outlook for hard-templated 3DCN-based materials.

Multi-scale hard template for 3DCNs

In 1988, the hard template was first introduced into the synthesis of carbon materials by Kyotani and his co-workers [16]. Since then, numerous types of templates have been developed, such as metal [17], salt [18], ice [19], silica [20], Metal-organic frameworks (MOF) [21] and so on (Fig. 1). Due to the different characteristics among various template materials, the corresponding productions present various architectural features, such as the specific surface area, pore size distribution, morphology, and even the macroscopic state of the products. We classify various hard templates according to the pore sizes of templates and corresponding products (Fig. 1) and review these templates based on their characteristics.

Metal template

The metals enjoy good plasticity and processability and can be made into numerous and designable shapes. As a result, the metal template is one of the most popular hard templates. In general, the use of metal templates is usually associated with gaseous or solid carbon precursors and high-temperature conditions. Assisted by the metal templates, the carbon precursors are pyrolyzed under high temperature and deposit carbon atoms on the metal surfaces. As a result, the carbon products will duplicate the delicate structure of metal templates. Herein, we will give some examples of these metal templates for synthesizing 3DCNs.

Metal foam template

Metal foam refers to a series of special metal materials with a three-dimensional porous structure, whose porosity is usually more than 95% [22]. Comparing with normal metals, the metal foams possess lighter weight in the same volumes and have good sound absorption, energy absorption, and electromagnetic shielding performance. Metal foam can be made of nickel, copper, iron or alloy materials [23,24]. Numerous researchers have work on using foam metal as a template to prepare 3DCN. One representative work was reported by Cheng’s group in 2011. They developed a general strategy to synthesize 3D graphene foams by using Ni foam as the templates [25] with a pore size up to millimeter scale. The procedures consisted of a chemical vapor deposition (CVD) followed with a chemical etching process. In the CVD process, CH_4 as the carbon source was decomposed at 1000 °C enabling atomic carbon dissolved in the Ni foam, and a consequent cooling enabled the phase segregation happened in the Ni-carbon interphase. The carbon atoms diffused to the surface of Ni and form graphene networks (Fig. 2a–d). This strategy successfully synthesizes the 3D macrosturctures of foam-like graphene, whose interconnected network serves as the fast electron transport channels and achieves a high electrical conductivity.

In this strategy, the template can be extended to other metal foams, such as copper [26] and silver [27], and the alternative car-

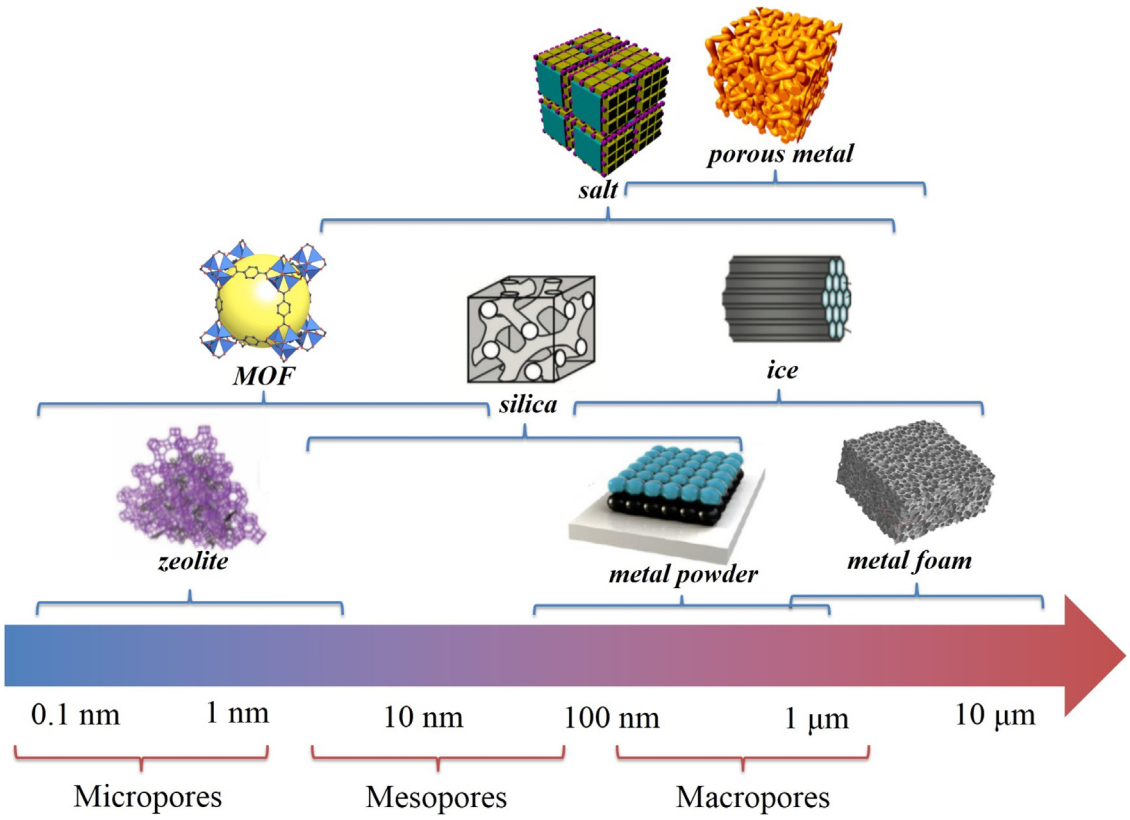

Fig. 1. The different types of hard templates and their corresponding length scales.

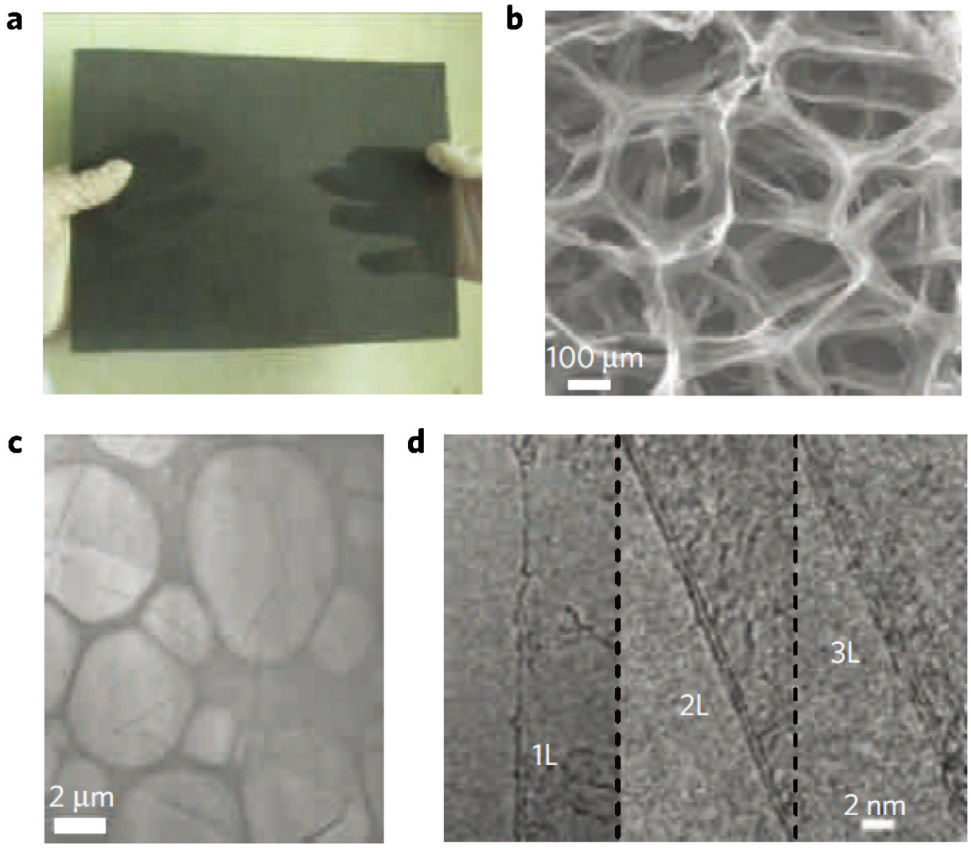

Fig. 2. (a) Photograph and (b) SEM image of (c,d) TEM image of a free-standing 3D graphene foam by Ni foam template (Reproduced with permission from Ref. [25], Copyright © 2011 Nature Publishing Group).

bon source precursors also include other organic gases (e.g., C_2H_2, C_2H_4), organic solvent (e.g., benzene [28]) and even solid carbon source (e.g. glucose and dicyandiamide). Moreover, heteroatom-doping in the final products could also be achieved by introducing impurity element raw materials into the precursors. For example, introducing NH3 as a nitrogen source can result in the N-doped 3D graphene [29].

Nanoporous metal template

Apart from the commercial foam, the metal frameworks with nanopores are also used as the templates for producing nanoporous 3DCNs. The origin nanoporous metals are obtained from AuAg binary infinite intersoluble alloys by de-alloying [30], then other intersoluble alloys are developed to reduce costs, such as Zn-Co [31], Cu-Pt [30], Cu-Ni [32] and Ni-Mn [33]. Recently, ternary alloys are also developed such as Ag-Au-Pt [34], Ni-Cu-Mn [35], Ni-Fe-Mn [36] and Mg-Cu-Al [37]. As an example, Chen's group fabricated a nanoporous Ni framework by a simple dealloying method by removing Mn from a $Ni_{30}Mn_{70}$ alloy foil [28]. As the residual, the Ni matrix has an interconnected nanostructure with ~20 nm pores. Incorporating this nanoporous Ni with the carbon source of pyridine, a free-standing 3D nanoporous graphene with open nanoporous channels was synthesized by a CVD process (Fig. 3a–d).

The nanoporous metal template approach has been extended to other metals, such as Cu. Qin et al. prepared a Cu matrix with continuous nanopores (NPC) by chemical dealloying a $Cu_{40}Mn_{60}$ alloy [38]. The graphene was grown on NPC by a short-time CVD method (at 900 °C for 2 min). In this process, Cu presents the surface-mediated growth for graphene, meaning that the carbon atoms directly assemble on the Cu surface instead of dissolving in the metal bulk. After removing the Cu matrix, a 3D graphene network with continuous duct-like structure (3D-DG) was obtained, exhibiting a real density of 0.15 mg cm^{-2} and high specific surface area of 586.3 m^2 g^{-1} (Fig. 3e–m). Additionally, this 3D carbon matrix showed an extremely low electrical resistance (23.3 Ω sq^{-1}) due to its duct-like structure-preserving the high electrical conductivity of graphene. This research highlighted that hydrogenated graphite (HG) can relieve the coarsening of NPC in the CVD process. Furthermore, the short-time CVD process can be employed in nanoporous Ni template for synthesizing a nitrogen-oxygen co-doped 3D nanoporous graphene (NO-3DNG) film as shown in Fig. 3n. Due to the decreased size of metal pores, the corresponding pore size of NO-3DNG was less than 20 nm (Fig. 3o–q). The active material loading of NO-3DNG film was up to 3.65 mg cm^{-2}, enabling an improved volume utilization of the material [39].

Metal powder template

Besides the above-mentioned top-down strategies, another roadmap to synthesize 3DCNs is the bottom-up method. By using catalytic metal powders as the templates, a 3D structural graphene can be obtained after removing metal templates. The pore size of 3DCNs was controlled by adjusting the size of metal particles. It has proved to be a good strategy by using metal powders as the templates, and the pore size can be tuned by choosing different sizes of raw material powders. To this regard, Sha et al. first demonstrated a simple technique to combine traditional powder metallurgy and CVD for fabricating free-standing 3D graphene foams (Fig. 4a) [40]. Ni powders and sucrose were mixed to obtain a pre-made powder mixture, which was then cold-pressed and heated to 1000 °C. During synthesis, Ni powders were sintered as the template and catalyst, and sucrose was decomposed and carbonized into graphene (Fig. 4b–e). The final product (PMT-GF) consisted of carbon shells and graphene layers display good electrical conductivity (13.8 S cm^{-1}). More importantly, this 3D graphene foam did not break even being compressed. To further control the pore size of the obtained 3D carbon, Garrido and colleagues prepared the templates by sintering metal powders at 600–1100 °C [41]. In their work, the density and the pore size can be changed by controlling the temperature and metal particle sizes. In addition, both of Ni and Cu were sintered to the templates with pore size down to 1 μm, and the produced 3D graphene had a similar size with these metal powders.

These metal powder templates have the advantage of uncomplicated pre-processes and easy to shape. Since the metal powders are potential raw materials for 3D-printing technology, it shows great potential to couple these two techniques in the synthesis of 3DCN-based materials. Sha and co-workers carried out an early exploration of metal-templated 3D-printing technology and successfully obtained a 3D-printed graphene monolith [42]. By mixing carbon source and Ni powders, the precursors were deposited on a stage and sintered by CO_2 laser in a laser cutter. As described in the metal powder template mechanism, the Ni powders catalyzed the carbon source decomposition for growing graphene. After removing the metal powders, researches obtained a 3D graphene foam (3D GF) with high porosity (99.3%) and good mechanical properties. This work verified that the laser can directly convert a solid carbon source into graphene and pave the way for the use of the hard template in state-of-the-art manufacturing technology.

Inorganic templates

Representative inorganic templates include silica, zeolite, salt, etc. Comparing with metal templates, inorganic templates can be used to manufacture 3DCNs on multiple scales from sub-nanometer to micrometer. Yet, most inorganic templates lack the catalysis ability on carbon atoms, they need high-temperature assistance to produce 3DCN with high quality and crystallinity.

Salt templates

Comparing with metal, the salts perform as low-cost *in-situ* hard templates and satisfy the requirements of large-scale production. In a typical synthesis, carbon precursors (e. g. glucose, sucrose, biomass) and inorganic salts (e. g. NaCl, Na_2CO_3, $ZnCl_2$, $CaCO_3$) are mixed together, and the followed carbonization processes convert the carbon precursors into carbon [18,43,44]. The salt template maintains its structure because of their chemical stability and then can be removed by a simple water-washing step, which is more environmentally friendly compared with the chemical etching of metal templates.

Recently, our group has developed a general strategy for producing 3DCNs based on NaX salts (X = Cl^-, CO_3^{2-}, SiO_3^{2-}) [18]. This salt assembly technique follows the basic steps: carbon precursor and salt were dissolved in water, and a freeze-drying process enabled the salt self-assembly with carbon precursors coated on the surface. This 3D composite was heated under certain atmosphere and the carbon precursors were converted into carbon nanosheets inside the nanoconfined space between salt surfaces. The salt templates were removed by water washing to obtain the final 3DCNs. Obviously, this method is characterized by their convenient preparation, environmental protection, and non-pollution. Moreover, the morphology of the carbon networks can be controlled by the selection of salt templates: the micrometer-scale pores were generated by NaCl particles; Na_2CO_3 particles resulted in the pore size of 50–100 nm, while the 5–10 nm nanopores were derived from the Na_2SiO_3 template (Fig. 5a–i). When mixing these three types of salts as multi-template, the corresponding 3DCN showed a hierarchical porous network structure, whose pore size distribution could be tuned by varying the ratios of these salts (Fig. 5j–m). For example, the combination of NaCl and Na_2SiO_3 were used as hierarchical templates to produce porous 3DCN. The corresponding carbon presents an interconnected cubic-like macropore network, which is constructed by mesopores carbon nanosheets. Elevating

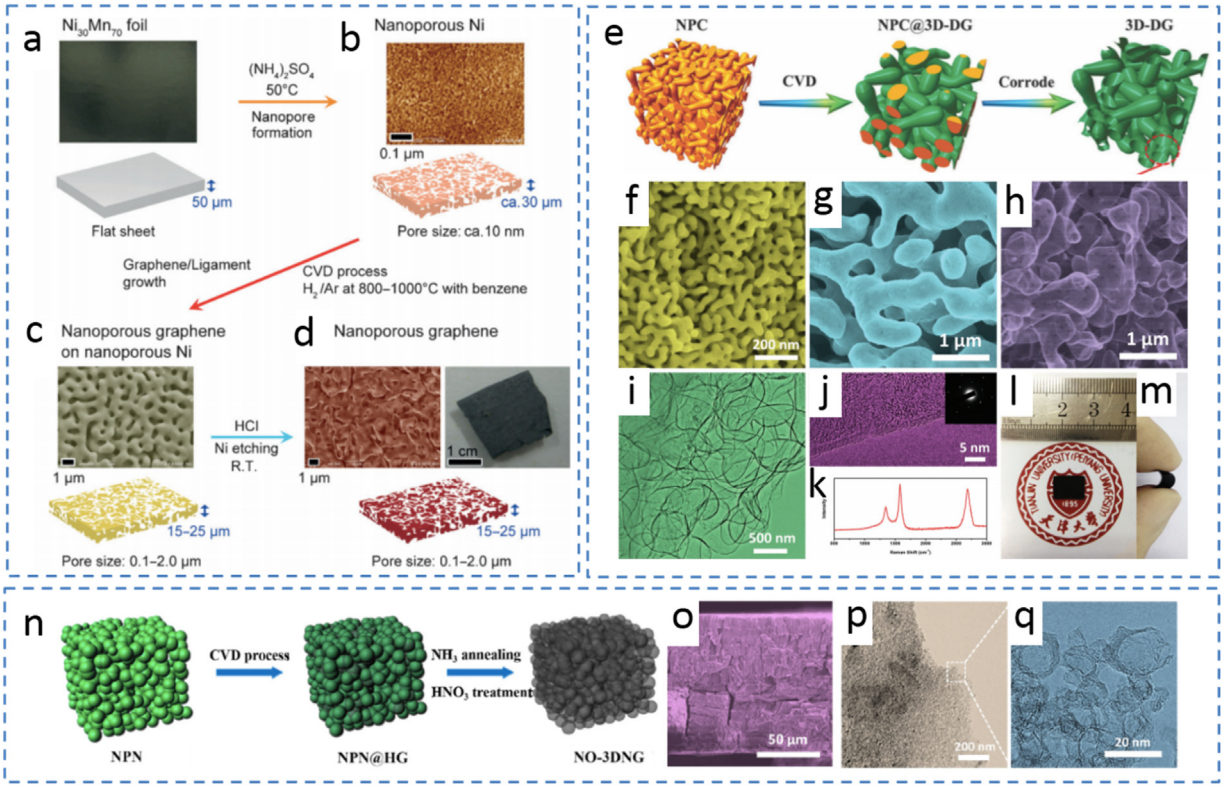

Fig. 3. (a) Image of $Ni_{30}Mn_{70}$ foil. (b) SEM image of nanoporous Ni after dealloying. (c) SEM image of nanoporous graphene on nanoporous Ni after CVD. (d) SEM and optical images of nanoporous graphene after removing the nanoporous Ni template (Reproduced with permission from Ref. [28], Copyright © 2014 Wiley-VCH). (e) Schematic of synthesizing 3D graphene by using Cu template (Reproduced with permission from Ref. [38], Copyright © 2016 Wiley-VCH). (f) SEM image of the cross-section of the de-alloyed NPC. (g) SEM image of NPC@3D-DG grown at 900 °C for 2 min. (h,i,j) SEM and TEM images, (k) Raman spectrum and (l,m) photographs of 3D-DG. (n) Schematic diagram of the fabrication of NO-3DNG film. (o) SEM image and (p,q) TEM images of the fabrication of NO-3DNG (Reproduced with permission from Ref. [39], Copyright © 2018 Elsevier).

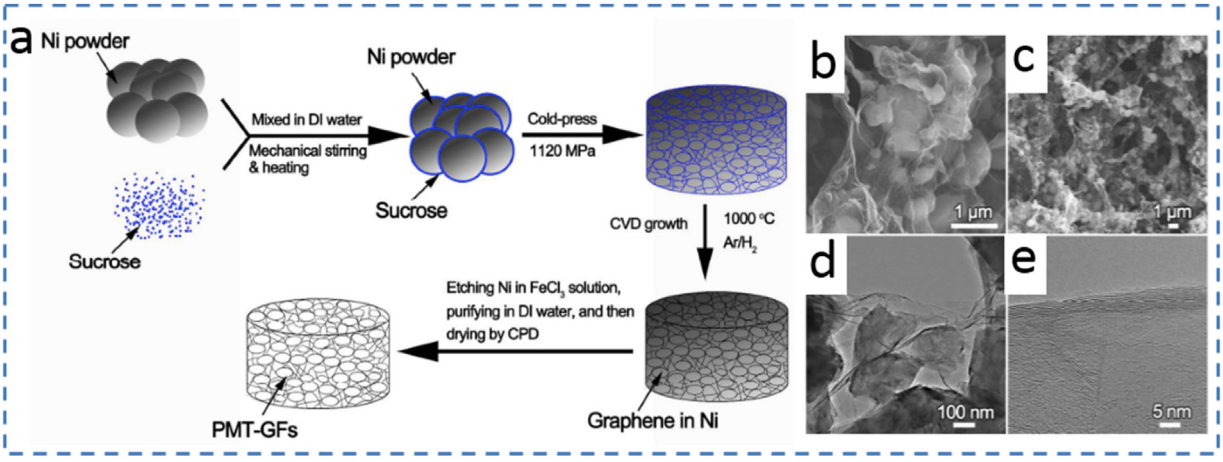

Fig. 4. (a) Schematics of powder metallurgy-chemical method to prepare 3D graphene foam. (b, c) SEM and (d, e) TEM images of as-prepared PMT-GFs (Reproduced with permission from Ref. [40], Copyright © 2015 American Chemical Society).

the ratio of Na_2SiO_3 from 2% to 4%, the mesopore size rises from 5 to 8 nm. In this process, the thickness of the carbon layers was also adjusted: increasing the proportion of salt reduces the thickness of carbon layers [44]. Thus, this salt template method can be applied in the production of a few layers of graphene. In the case of $ZnCl_2$/NaCl salts [45], by controlling the ratio of the two salts, the high pore volume of 5.2 $cm^3\ g^{-1}$ and specific surface area of 2540 $m^2\ g^{-1}$ were achieved. Furthermore, by adding the corresponding heteroatom source in the precursors, this method can be extended to synthesize heteroatom-doping (e.g. N, O, S) carbon materials [44,46,47].

The organic salts also can act as the multifunctional templates to fabricate heteroatom-doping carbon networks. The researcher applied ethylenediaminetetraacetic acid disodium zinc salt ($EDTANa_2Zn$) as a hard template. During heating the mixture of salt and carbon sources, $EDTANa_2Zn$ will produce the nano-ZnO and Na_2CO_3 particles, which are evenly dispersed in the carbon sources. Na_2CO_3 can serve as a template to create mesopores, and the nano-ZnO can etch carbon as an activation agent to deliver the micropores and small mesopores. Moreover, the decomposition of $EDTANa_2Zn$ can introduce nitrogen-doping in the carbon matrix. Because of the

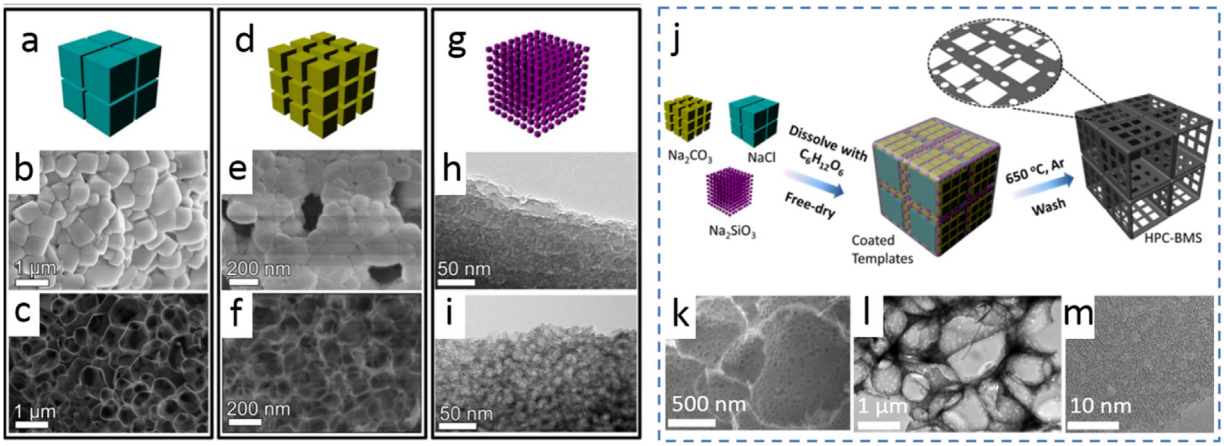

Fig. 5. (a) Schematic of NaCl template, (b) SEM image of carbon-coated micro-sized NaCl and (c) the obtained 3DCN after washing step. (d) Schematic of Na_2CO_3 template, (e) SEM image of carbon coated Na_2CO_3 and (f) the obtained 3DCN after washing step. (g) Schematic of Na_2SiO_3 template, (h) SEM image of carbon coated Na_2SiO_3 and (i) the obtained 3DCN after washing step. (*j*) Schematics demonstrating the fabrication process of carbon (HPC-BMS) with the assistance of multi-scale soluble salt self-assembly. (k) SEM, (l) TEM and (m) HRTEM images of HPC-BMS. (Reproduced with permission from Ref. [18], Copyright © 2015 Royal Society of Chemistry).

multifunction of this salt template, the obtained carbon shows the hierarchical porous structure, large surface area (2160 $m^2 g^{-1}$) and nitrogen doping [48].

Silica templates

The 3DCNs synthesized by salt templates often present pores with a certain distribution range. To synthesize the carbon materials with regular pore structure (2–50 nm), silica templates, such as MCM-48 and SBA-15, were the better choice [15,49–51]. For example, the carbon materials derived from MCM-48 have the mesopores of 2–10 nm [15,49]. The typical process of this template method is similar to the metal template, including the precursor immersion, carbonization and template removal [52]. However, the removal of the silica-based templates usually uses HF or NaOH concentrated solution, instead of an acid solution for metal templates or water for salt templates (Fig. 6a) [53]. Moreover, Schuster et al. applied a phenol and formaldehyde mixture precursor to synthesize spherical 3D mesoporous carbon structure by using spherical silica as the template. The obtained carbon exhibited a bimodal pore size distribution with average pore diameters of 6 and 3.1 nm [54,55].

Besides mesoporous silica, silica particles can also be applied to fabricate 3D carbon matrix [56]. Huang et al. used methyl functionalized silica particles (30–120 nm) as templates [57]. They mixed the silica spheres and GOs in a neutral aqueous solution, and these two materials would assemble to form a 3D mixture due to the hydrophobic interaction. This composite was then annealed to reduce GOs and followed by the removal of silica templates (Fig. 6b). Moreover, the continuum of silica can be used as a template for 3DCN. Backov's group produce a silica monolith Si(HIPEs) with interconnected structure by a sol-gel method [58]. Then, they used this Si(HIPEs) as a hard template to produce an interconnected macro/microporous carbon monolith (Fig. 6c–g). This carbon monolith demonstrates a specific surface area above 600 $m^2 g^{-1}$ and the conductivity of 20 S cm^{-1}, which has excellent mechanical properties (Young's modulus of 0.2 GPa) and can be cut and shaped easily.

Zeolite template

To further decrease the pore size of 3DCNs to the micropores, the zeolites are used as the hard templates [59,60]. Zeolite is a series of aluminosilicate porous solid, which possess 3D interconnected nanochannels, such as zeolite X, zeolite Y and EMT-type zeolite [61]. Carbon sources can be introduced into the zeolite nanochannels by polymer-impregnation followed by carbonization and/or CVD process. After removing the zeolite, the zeolite-templated carbons (ZTCs) were obtained (Fig. 7a–c) [62]. These ZTC present higher volumetric surface area and particle density than those of the 3D carbon materials produced by using other templates.

There is a hindrance to the application of zeolite-based synthesis that the filling of carbon sources into nanopores of zeolite (<1.5 nm) is difficult. This issue was partially solved by conducting a pulsed chemical vapor deposition. Enabled by this improved technique, a 3D ordered microporous carbon with a surface area of 2100 $m^2 g^{-1}$ was produced in the confined nanochannels of zeolite Y by using acetylene gas through [63].

To further optimize the process of preparing 3DCNs from zeolite template, Kim's group applied lanthanum ions embedded in zeolite pores, and lower the temperature required for the carbonization of ethylene or acetylene [64]. Therefore, a carbon framework was formed along the walls of micropores in the zeolite, which was supported by X-ray diffraction data from zeolite single crystals after carbonization (Fig. 7d–f). This ZTC possesses the superior electrical conductivity: the value is two orders of magnitude higher than that of amorphous mesoporous carbon.

Other hard templates

In addition to the metallic and inorganic templates, there are a lot of hard templates, such as MOF, ice, metal oxides, metal sulfides, metal nitrides, metal carbides and so on [65], and we focus on two of them.

MOF template

As a novel class of nanoporous materials, MOF is a kind of framework structures constructed by transition-metal clusters and organic ligands [66–70]. Due to their high specific surface area and large pore volume, several kinds of MOFs, such as MOF-5, Al-PCP, and ZIF-8, have been considered as promising precursors to construct 3D carbons with nanopores [71–73]. Xu and co-workers applied a vapor phase protocol to introduce furfuryl alcohol (FA) into the nanopores of MOF-5 [74]. Consequent carbonization at 1000 °C enabled the formation of nanoporous carbon with a high specific surface area of 2872 $m^2 g^{-1}$. When decreasing the temperature, the carbon material presents much lower specific surface areas of 417 $m^2 g^{-1}$ at 800 °C and 217 $m^2 g^{-1}$ at 503 °C. This work verified that MOFs can serve as the sacrificial templates for synthesizing 3D nanoporous carbons, and figured out the influence of

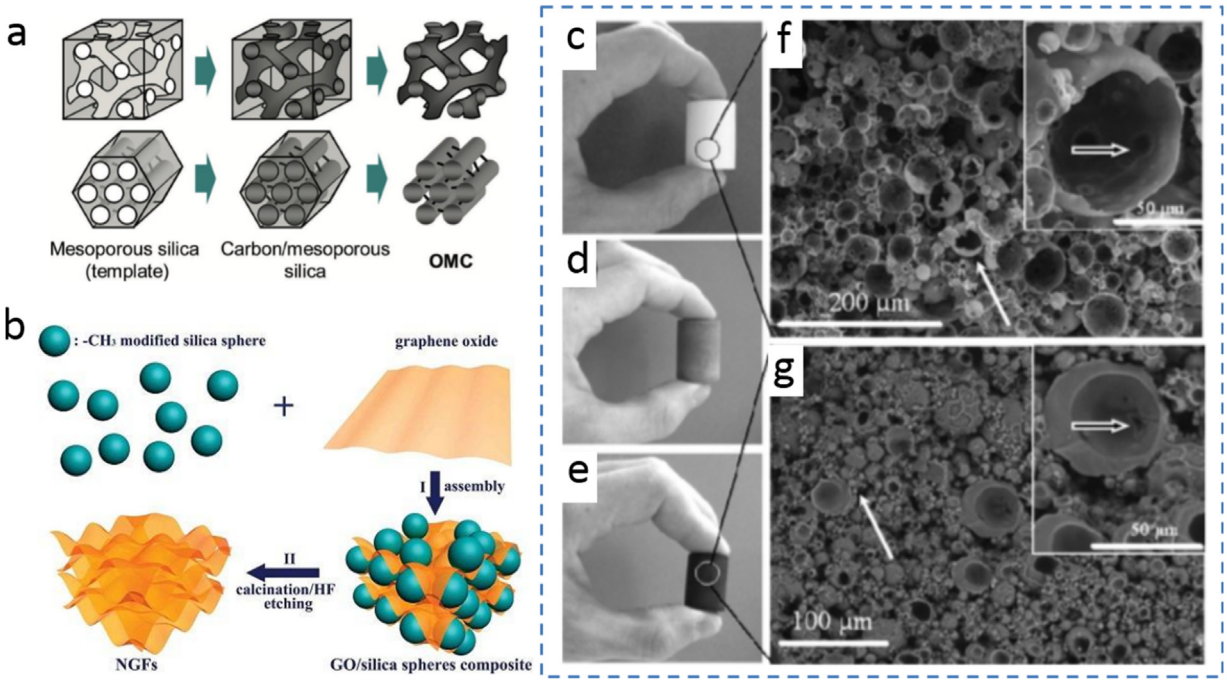

Fig. 6. Schematics demonstrating the fabrication process of 3DCN by (a) mesoporous silica (Reproduced with permission from Ref. [15], Copyright © 2012 Wiley-VCH) and (b) silica nanospheres (Reproduced with permission from Ref. [57], Copyright © 2012 Wiley-VCH). (c) silica porous Si(HIPE) template [58]. (d) cross-linked precursor/silica-template hybrid composite, and (e) resulting in carbon material after carbonization and silica removal. (f) SEM of Si(HIPE) template and (g) SEM of the resulting carbon (Reproduced with permission from Ref. [58], Copyright © 2009 Wiley-VCH).

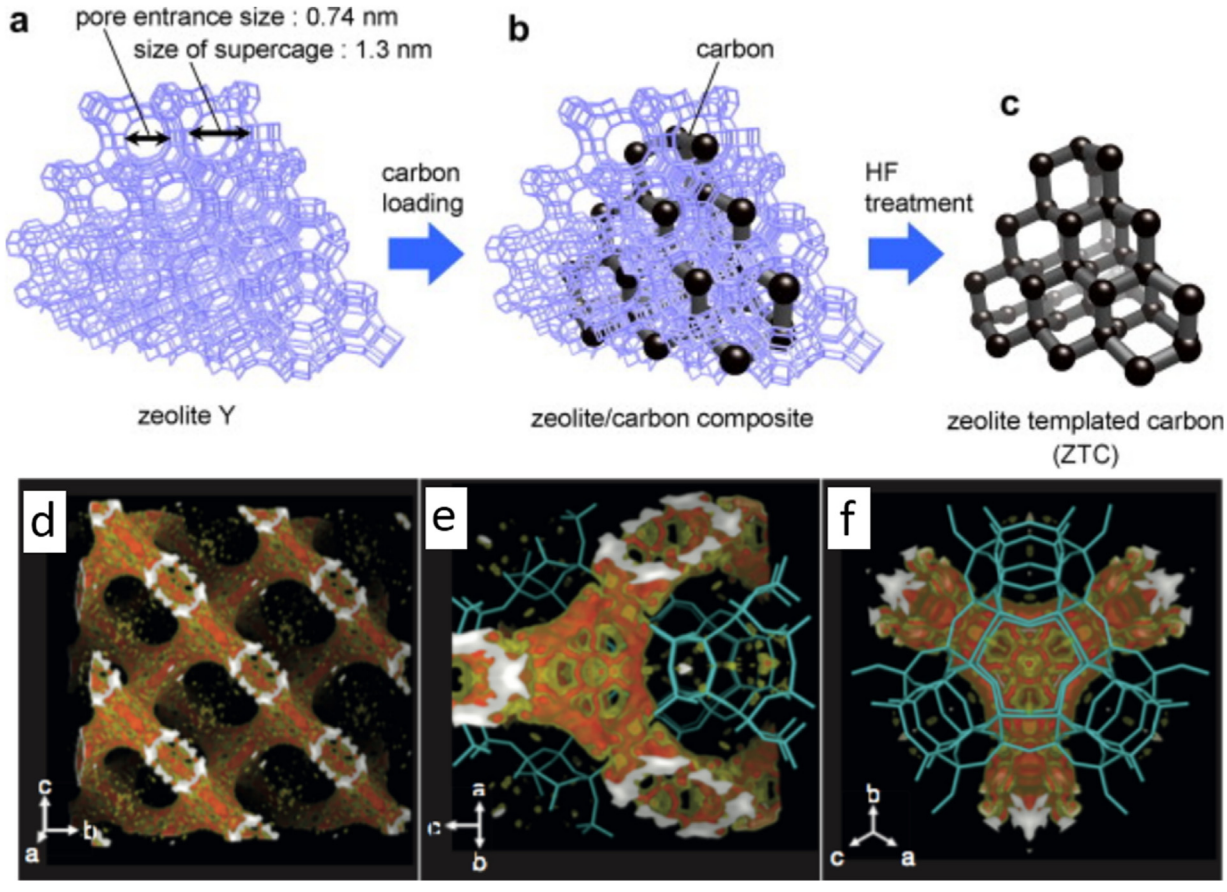

Fig. 7. Synthesis procedure of ZTC: (a) crystal structure of zeolite Y, (b) zeolite/carbon composite, and (c) the framework of ZTC (Reproduced with permission from Ref. [62], Copyright © 2009 Elsevier) (d) 3D electron-density map of the carbon framework excluding the zeolite FAU. (e,f) Enlarged images of the electron-density map, including the zeolite FAU (cyan), from different viewpoints: along the (110) axis (e) and the (111) axis (f) (Reproduced with permission from Ref. [64], Copyright © 2016 Nature Publishing Group).

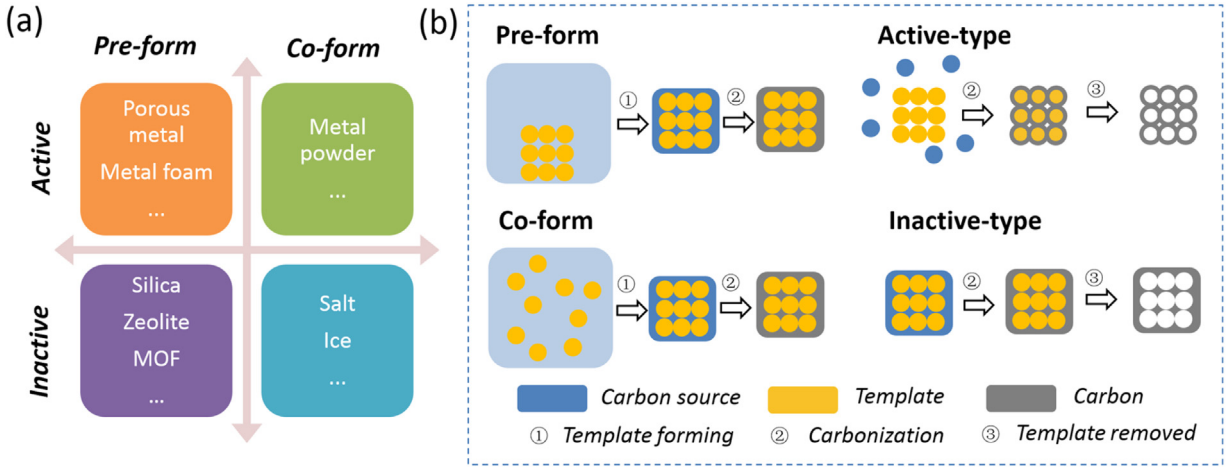

Fig. 8. (a) The hard templates are divided into four quadrants according to their characteristics. (b) The details of processes for pre-form and co-form templates, as well as active-type and inactive-type templates.

heating temperature on the morphology of the as-obtained carbon as well. Yamauchi et al. demonstrated that FA can also be immersed in Al-PCP and converted into porous carbon with a specific surface area of 513 $m^2 g^{-1}$ [70]. Besides, many kinds of carbon sources can be combined with MOF template, including glycerol, carbon tetrachloride, ethylenediamine and phenolic resin [70]. Furthermore, the structure of 3DCN can be obtained by calcining MOF itself directly, because the organic component in MOF is used as a carbon source, and the inorganic component acts as the template and catalyst. In this aspect, by assembling the particles of a microporous ZIF-8, 3D carbon with micro-, meso- and macropores was prepared by ultrasonication and consequent carbonization [21]. This research demonstrates that the secondary voids of MOF nanoparticle can be used as "mesoporous" template. Besides, the effort has been made to prepare different kinds of MOF structures. For example, researchers synthesize the superlong single-crystal MOF nanotubes. Then, hierarchical structure carbon nanofibers wrapped by carbon nanotubes are formed by the carbonization of the Co-MOF nanotubes along with dicyandiamide [75]. Great progress has been made to control the structure of MOF and MOF-derived materials, and the relationship between their structure and the physico-chemical properties have been reviewed in relative articles [66,67].

Ice template

As the typical *in-situ* template, ice templates are used for producing 3DCNs and can be regarded as the most inexpensive one among various hard templates [76]. To use ice template, the soluble carbon precursors are dissolved in water and froze at low temperatures. In this process, the growing ice-crystals repel the carbon precursors in the space of ice particles [77]. After removing ice, the arrangement of concentrated precursors is maintained, and the pores are the negative replica of the ice-crystals. This versatile method has been used to produce carbon materials and their composites [78]. For example, a kind of 3D macroporous carbon monolith has been fabricated by using an ice-rod template [79]. The authors found that the ice template assembled as an array of nanorods during the freezing process, and the consequent carbon monolith exhibited a honeycomb-like morphology with 180 nm pores. Furthermore, this macroporous architecture can be tuned by adjusting the freezing conditions and precursors amount. As one advantage of the ice-template strategy, the starting materials can be an extremely dilute suspension, which can be applied to produce many kinds of carbon-based aerogels, such as carbon nanotube, graphene oxide, porous carbon and their composites [19,76,80]. To this regard, the ice-template was applied to synthesize macroporous graphene monolith with a density as low as 0.14-0.16 mg cm^{-3} [76] (Table 1).

Table 1
Characteristics of various hard templates and their corresponding carbon products.

Type	Removal	Price	Example	Products state
Metal foam	Acid solution	Middle	Ni foam	Monolith
Porous metal	Acid solution	High	Porous Cu	Monolith
Metal powder	Acid solution	Middle	Ni/Cu powders	Powder/Monolith
Salt	Water	Low	NaCl, Na_2CO_3	Powder
Silica	NaOH, HF	Middle	Silica sphere	Powder
MOF	Acid solution	High	MOF-5, ZIF-8	Powder
Zeolite	HF	Middle	Zeolite X/Y	Powder
Ice	Water	Low		Powder/Monolith

Up to now, we have introduced various templates based on their components, such as metal and inorganic materials. Based on the above review, we find that these different types of templates have some common features in the aspects of 3DCNs' growth mechanism and the generation of hard templates. As shown in Fig. 8, we can classify these hard templates into four quadrants. Firstly, two types of hard templates can be summed up according to their catalytic activity for carbon: the active-type and the inactive-type. For the active-type templates, the used materials are catalytic for the carbon precursors, such as most of the metal templates, meaning that the templates can provide their catalytically active surface for carbon atom assembling [81]. As a result, the gaseous carbon sources are often applied with the active-type templates. By comparison, the inactive-type templates lack the catalytic activity for carbon atoms and require the solid or liquid precursors for filling into the space of the substrates [59]. As a typical example of inactive-type templates, Kyotani et al. used zeolite Y as a template and FA as a carbon source to synthesize the 3D nanoporous carbon with the nanocasting and carbonization [82].

In another dimension, the hard template can be classified into pre-form templates and co-form templates based on their formation processes. The 'pre-form' means that the template is prepared before mixing with carbon precursors. The above-mentioned templates, such as porous metal, metal foam, silica, MOF and zeolite, belong to the type of pre-form template [83,84]. The 'co-form' refers that the templates are forming concurrently during the carbon synthesis processes [85,86]. In this aspect, the typical examples are the soluble salt and salt applied as templates for fabricating 3DCNs.

Although we provide such a classification, we have to say that there are too many kinds of hard templates to give simple

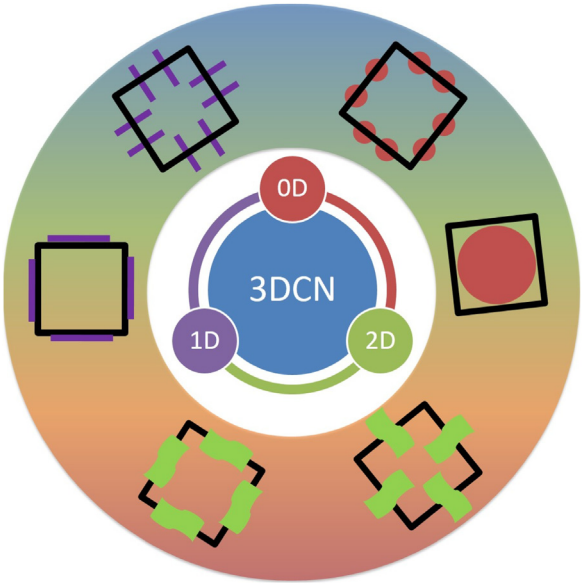

Fig. 9. The schematic of 3DCNs and their multi-dimensional nanomaterial composites. 0D nanomaterials.1D nanomaterials: 2D nanomaterials.

dichotomy. In this classification, we try to extract the commonalities of various templates, so that readers can have a general guide in screening templates during their experimental designs. In practice, the basis for template selection is which one is helpful to prepare the required structures, to meet the experimental conditions, and to reduce the cost as much as possible.

Synthesis of 3DCN composites based on hard-templates

The composite material is the combination of various components and optimized by advanced material preparation technology, which is the current development direction in the field of structure and function applications [87–89]. Because of the advantages of large specific surface area, high electrical conductivity, and high connectivity, 3DCNs can combine with other nanomaterials to achieve the synergistic benefits (Fig. 9). Therefore, 3DCNs can be used as both the reinforcement of composite materials and the matrix of composite materials to meet different application needs. This section introduces 3DCN-based composites prepared from hard templates. Several examples of 3DCN composites using the hard template method in recent years are listed in Table 2. As can be seen, the 3DCNs can be composited with numerous types of nanomaterials, from carbon materials, metal oxides to metal sulfide. Moreover, the weight percentage of these second components ranges from 5% to 90%, ensuring a great potential for controlling the overall properties of these composites. In addition, it should be pointed out that the high temperature is required in all hard-template method to achieve a carbonization process, which indeed increases the energy consumption and process complexity of these methods.

In order to systematically review these 3DCN-based composites, we choose the morphology features of the second components as the classification basis and classify the second components into 0D, 1D and 2D materials (Fig. 9).

DCNs/0D composites

The typical 0D materials include single atoms, nanoparticles (NPs) and even spherical nanomaterials. Firstly, the isolated single-atom catalysts have attracted great interests in electrocatalysis since they have the maximized atom utilization efficiency. To this regard, a simple hard template method is reported to synthesize carbon networks containing metal atoms (e.g. Ag, Rh, Ir, and Pt) [113]. Firstly, the target metals and carbon precursors were introduced into the zeolite template by wetness impregnation, and the nanospace of zeolite can capture these metal atoms. After the carbonization, the metal/3DCNs composites were obtained. Also, the characteristics of ZTC can influence the mass loading of metal atoms. It has been approved that S-doped ZTC can achieve 5 wt% platinum loading in the carbon matrix [96]. Also, a SiO_2 template method is applied to fabricate the isolated Fe single atomic anchoring on graphene hollow nanospheres (Fe ISAs/GHSs) (Fig. 10a,b). In the precursor, the Fe phthalocyanine has planar macrocycle structure, which exhibits the steric hindrance effect with graphene and resulting in the atomic dispersion of Fe-Nx species. As a result, the obtained sample shows the morphology of the 3D sphere with the Fe single atoms anchoring on the carbon walls (Fig. 10c–e) [114].

Meanwhile, the metal NPs have attracted attention due to their high chemical activity in numerous reactions. Using capsular MOF and melamine as precursors, Xu et al. reported iron-nickel phosphide nanoparticles immobilized on capsular carbons interconnected by plentiful carbon nanotubes [115]. Our group reported a strategy to synthesize 3D porous graphene networks anchored with Sn NPs (Sn@G-PGNWs) [91]. This method uses metal precursor as a catalyst and self-assembled NaCl as a template. In the process, freeze-drying enables a film of $SnCl_2$ and carbon source confined in the space between NaCl particles, and the following calcination reduces the metal precursors into Sn NPs (5–30 nm), which act as a catalyst for graphene growth. As a result, the graphene formed not only in the space between NaCl particles but also on the Sn surface. The obtained 3D Sn@G-PGNWs depicts good conductivity and high specific surface area, in which the NPs are tightly pinned on the surfaces of thin walls of 3D graphene. This method is further extended to other NPs such as Co_3O_4, Fe_2O_3, NiO, MnO_2, $Ni(OH)_2$, etc. [93,116–118].

The definition of 0D nanomaterials is not only regarded as the NPs smaller than 10 nm but also refers to the materials with 0D architectures. For example, our group has founded the 3DCN with macropores produced by using salt template can play an important role in the growth of MOF particles [103]. 3DCN can provide nucleation sites for the MOFs particles and result in the heterogeneous nucleation effect. Furthermore, 3DCN can exert its confinement effect when MOFs grows too large. As a result, the obtained MOFs particle size is much smaller than that without the carbon network (Fig. 11).

DCNs/1D composites

There are two types of assembling forms between 1D nanomaterials and 3DCNs. The first type is that 1D nanomaterials were attached to the surface of 3DCNs with a line-to-face connection [119]. In this respect, 1D materials serve as the reinforcements to enhance the mechanical or electrochemical properties of 3DCNs. The second type is point-to-face type, referring that 1D nanomaterials (e.g. metal oxide nanowires) were anchored on 3DCNs with their tips [108]. As a result, the role of 3DCNs is to provide a continuous conductive substrate for improving the overall performances of composites.

For the line-to-face typed 1D/3D composites, Sha et al. [107] reported a powder metallurgy strategy to fabricate a 3D carbon hybrid of graphene and CNTs inspired by rebar graphene work of Tour's group. For this purpose, a mixture of Ni powder, sucrose, and surface-modified CNTs was cold-pressed and then calcined at a high temperature. During this process, a 3D rebar graphene foam (3D rebar GF) material was grown *in situ* in one step. The shape of the composite foam can also be adjusted by changing the shape of the pre-formed block, as shown in Fig. 12a–c. Zhu et al.

Table 2
Recent achievements of 3DCN-based composites.

Second component	Features of second component	3DCN's type	Temp. (°C)	SSA# ($m^2 g^{-1}$)	wt %	Template	Ref
SnSb alloy	1-3 nm	3D N-doped porous graphene	750	219.8		NaCl salt	[90]
Sn NPs	5-30 nm	3D graphene	750	365	46.8	salt	[91]
Fe_2GeO_4 NPs	1-5 nm	N-doped carbon network	500	257.6		salt	[92]
MnO NPs	50-100 nm	Continuous carbon nanosheets	650	330	25.20	salt	[93]
SiO_2 NPs	70 nm	Porous carbon			22	salt	[94]
Co_9S_8 NPs		3D graphene	120			Ni foam/MOF	[95]
RuO_2 NPs	3-5 nm	N-3D graphene		188.7	55-75	Ni porous metal	
Pt atom	atomic scale	ZTC	800	2800	5	NaX zeolite	[96]
$LiBH_4$ NPs		ZTC	900	11.79		zeolite	[97]
Carbon nanocage						porous metal	[98]
Pt		3D Graphene				ice	[80]
SnO_2 NPs	3-4 nm	3D Graphene	350	237.7	40.20	ice	[99]
Cu_2Se NPs		3D MOF-derived Carbon	700	68.85	56	Cu-MOF	[100]
Fe_7S_8 NPs		3D MOF-derived Carbon	450	42.72	44	Fe-MOF	[100]
NiSe NPs		3D MOF-derived Carbon	450	64.79	82.60	Ni-MOF	[100]
Co_3O_4 NPs	5 nm	3D porous carbon network	550	217.4	49	MOF and Salt	[101]
WC_x NPs	5-50 nm	3D mesoporous carbon	900	433	30	silica	[102]
ZIF-8	0.2-1 μm	3DCN	650	1361	33	Na_2CO_3 salt	[103]
CNTs	10 nm diameter	3DCN	650	462		NaCl salt	[104]
Ag nanowire		3D-GC and mesoporous carbon	350	484	4.7	Ni foam	[93]
Co_3O_4 nanowire	100-150 nm diameter	3D N-doped carbon foam	180		61	metal foam	[105]
Co_3O_4 nanowires	200-300 nm diameter	3D graphene	1000			metal foam	[106]
CNT		graphene	1000	80		Ni powder	[107]
NiCo-LDH nanoneedle	10-20 nm diameter	3D graphene	900	405		Porou Cu	[108]
MoS_2 nanosheets	thickness<3nm	porous carbon networks	750	355		salt	[109]
graphene	thickness<3nm	3DCN	650	498.5		Na_2CO_3 and Cu	[110]
$Ni(OH)_2$ nanoplates	120 nm	3D graphene	180			metal foam	[111]
$CoMoO_4$ nanosheets	thickness<2nm	3D GF				Ni foam	[112]
MnO_2 nanosheets	100-200 nm	3D-DG	900			porous metal	[38]

SSA: specific surface area.

demonstrated a one-pot strategy for fabricating 3D B/N-doped networks of CNTs/carbon nanosheets hybrids [108]. To produce this 1D/3D carbon hybrid, NaCl serves as templates, and the hydroxyl single-walled CNTs and organics are space-confined in the gap of salt particles. After heating and removing the templates, the CNTs remained in the B/N-doped carbon nanosheets in the obtained sample (Fig. 12d–f).

The point-to-face typed composites were mostly fabricated by two-step methods. A continuous 3DCN is first prepared by hard template, and then a functionalized 1D structure is grown by a subsequent method means, such as hydrothermal. As a typical example, NiCo-layered double hydroxide (NiCo-LDH) nanoneedles were demonstrated to grow on a 3D rivet graphene (H-3DRG) film [108]. During the processing, a hydrothermal method enables the $NiCo_2S_4$ nanostructures grown on the H-3DRG (Fig. 12g–i). This research further proves the flexibility of 3DCN substrate.

DCNs/2D composites

2D materials have received extensive attention and research over the past decade due to their unique structural, mechanical and physical properties and potential applications. 3DCNs were combined with a large family of 2D materials includes 2D crystals of single elements (such as graphene), metal oxides, metal disulfides, etc. [7,120]. The fabrication of 2D/3D carbon hybrid is rarely reported because of the difficulty of seamlessly connecting of these two architectures. To tackle this issue, our group demonstrated the important role of the hard template. By combining two kinds of the template (Cu and Na_2CO_3), a graphene-reinforced N-doping porous carbon network (N-GPC) was successfully fabricated [110]. In this approach, the Na_2CO_3 is dissolved with glucose and urea and then dipped in a Cu substrate. A subsequent heating process enables the carbon precursor to convert into porous carbon copying the pattern of salt assembly. Meanwhile, wave-like graphene is formed at the interspace between metal and salt. This graphene layer not only increases the electronic conductivity but also enhances the structural stability for engaging the material with free-standing feature (Fig. 13a–d). According to the molecular dynamics simulation, the nanospace between Cu and salt conduct a heterogeneous space-confined effect, which is favorable to the atomic rearrangement of carbon and the formation of graphene.

Another connection type of 2D and 3D nanostructure is that 2D nanosheets attach on the wall of 3D networks to achieve a face-to-face contact. Zhou et al. demonstrated a 2D spatial confinement strategy to *in situ* synthesize MoS_2 nanosheets anchored on 3D porous carbon networks (3D FL-MoS_2@PCNNs) [109]. The key role in this strategy is NaCl, which not only serves as a template for growing 3D carbon networks but also provides a 2D-confined space for constructing few-layer MoS_2 nanosheets. In the prepared 2D/3D composite, the face-to-face contact between MoS_2 and carbon nanosheets can effectively avoid the aggregation and restacking of MoS_2 nanosheets (Fig. 13e–g). Besides, the typical 2D nanosheets of MnO_2 were vertically anchored on 3D nanoporous graphene (3D-DG@MnO_2). This hybrid was synthesized through an electrodeposition technique with 3D-DG as the matrix (Fig. 13h–j) [38]. The 3D-DG not only ensures a high electron and ion transfer but also allows a large MnO_2 mass loading of 90.5 wt% based on the entire electrode.

Energy storage applications of 3DCN composites

Because of their excellent physical and chemical properties, 3DCNs and their composites have shown excellent performance in a series of electrochemical energy storage, such as metal ion batteries, supercapacitors, and fuel cells, etc [121,122].

Battery

Nowadays, batteries are the most popular energy storage applications in electric cars, computers, mobile phones, and other electronic products. Several types of rechargeable batteries show great potential in energy storage, such as lithium-ion batteries

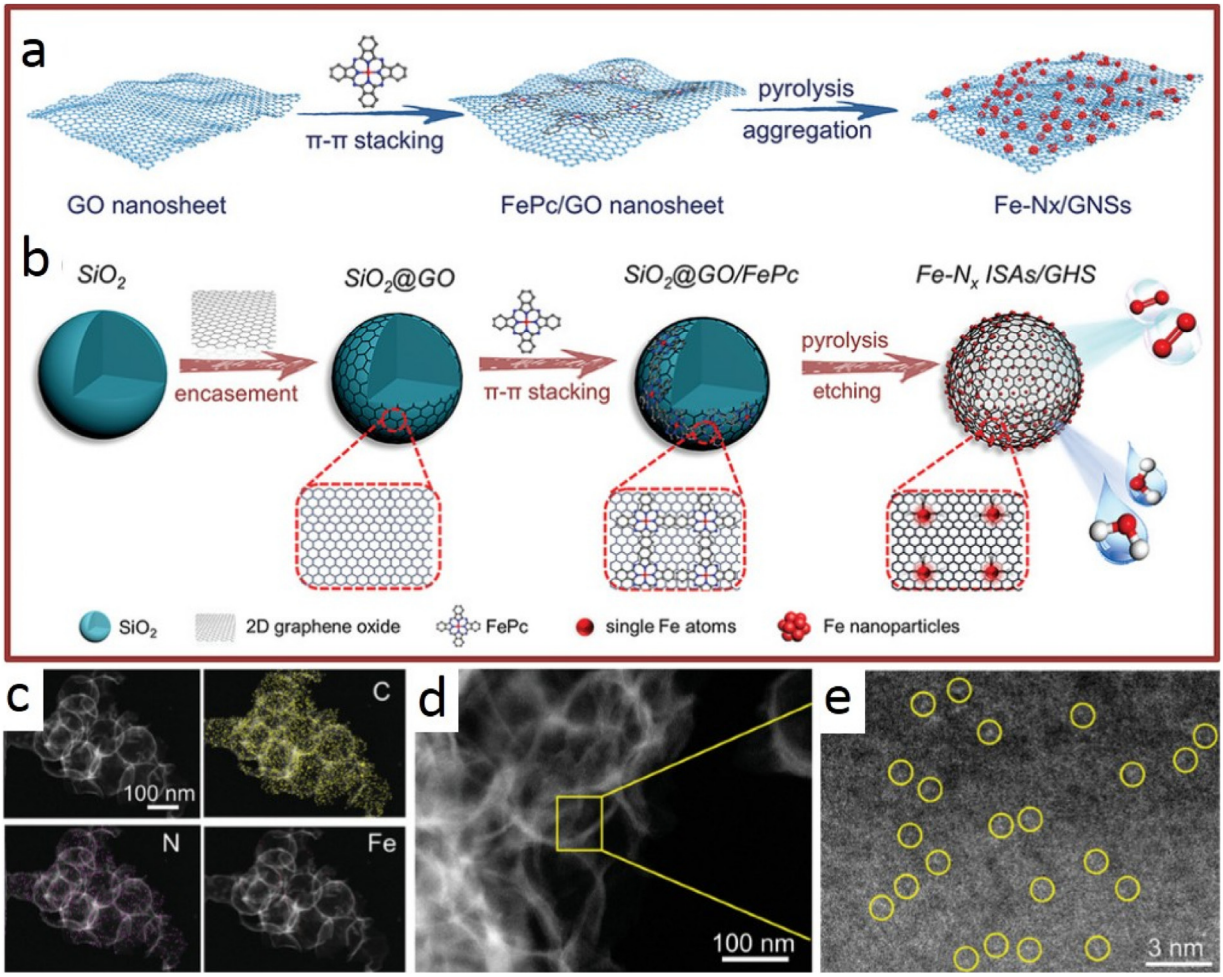

Fig. 10. (a,b) Schematic illustration showing the formation of Fe single atoms on graphene hollow nanospheres. (c) Elemental mapping images, (d,e) AC-HAADF-STEM images of Fe–Nx ISAs/GHSs (Reproduced with permission from Ref. [114], Copyright © 2019 Wiley-VCH).

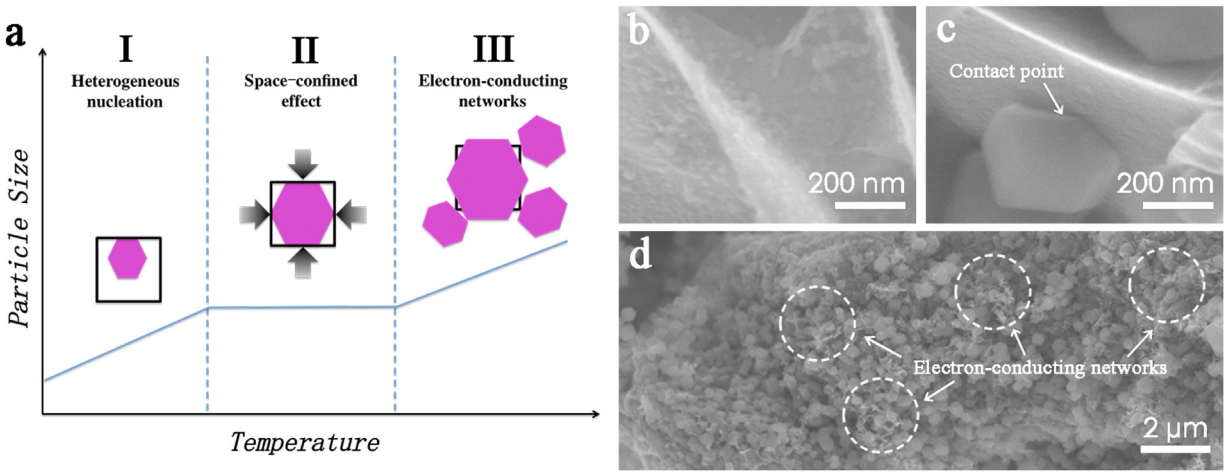

Fig. 11. (a) The three functions of 3DCNs in the fabrication of MOF/3DCN composites. (b) The SEM images of heterogeneous nucleation MOFs at the surface of 3DCN. (c) The contact point of the MOFs particle and the carbon layer. (d) The electron-conducting networks of 3DCN in the composite electrodes (Reproduced with permission from Ref. [103], Copyright © 2017 Royal Society of Chemistry).

(LIB), sodium-ion batteries (SIB) and lithium-sulfur (Li-S) batteries [123–127]. A typical battery configuration consists of anode, cathode, electrolyte and current collector. 3DCN and their composites produced by hard templates contribute a lot to enhance these components.

Due to the high electron conductivity of 3DCNs, it was interesting to apply 3DCNs to enhance the performance of the cathode electrode. Rouff's group used graphene foam (UGF) produced on Ni foam as current collectors to replace the traditional Al in a battery [128]. Then, the $LiFePO_4$ NPs were deposited on this UGF and

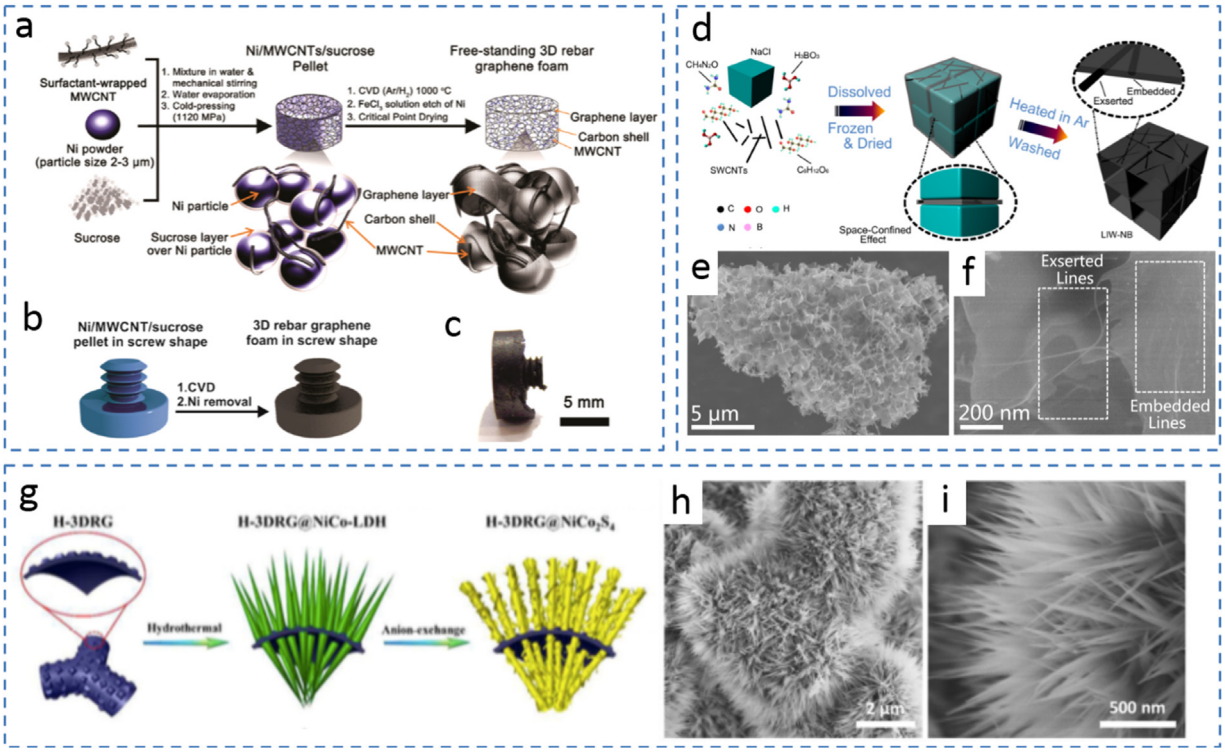

Fig. 12. (a) Schematic of powder metallurgy-chemical method to prepare 3D rebar GF. (b) Schematic of tuning the shape of the pellet to prepare 3D rebar GF into a screw shape and (c) its photograph (Reproduced with permission from Ref. [107], Copyright © 2017 American Chemical Society). (d) Schematic illustration of the salt template synthesis process of hybrid of 3DCN and carbon nanotube with (e, f) the corresponding SEM images (Reproduced with permission from Ref. [104], Copyright © 2016 Elsevier). (g) Schematic of the production and (h, i) SEM images of NiCo-LDH nano-needle on 3D graphene (Reproduced with permission from Ref. [108], Copyright © 2018 Royal Society of Chemistry).

exhibited a near theoretical capacity (170 mA h g^{-1}). Moreover, the hysteresis between the charge and discharge curves of $LiFePO_4$ on UGF was 30% less than that with Al current collectors (Fig. 14a–b). This research work plays the advantage of UGF's excellent electron conduction. Also, owing to the large free space inside UGF, it is a good substrate for loading other functional materials.

Among many energy storage devices, LIB is the most popular at present. The anode electrode of traditional LIB is graphite. Yet, the specific capacity of graphite is limited at 372 mA h g^{-1}. Therefore, a variety of new materials have been used in the LIB anodes, such as metal oxides, metal Sulfides, alloy and carbon-based composite [127,129,130].

In the application as anode materials, there are numerous examples. We have chosen one of the examples as an introduction. Sn has an ultrahigh theoretical capacity of 993 mA h g^{-1} yet suffers from the issue of volume change during the charge/discharge process [131]. To this aspect, 3DCNs can serve as the buffers to tackle with this problem. As mentioned earlier, Sn NPs were attached to the 3D graphene frame by a one-step *in-situ* template method (Sn@G-PGNWs) [91]. In the case of Sn@G-PGNWs composite, the CVD-synthesized carbon shells provided Sn NPs from the exposure to the electrolyte. Moreover, the carbon matrix can preserve the structural stabilization of Sn NPs and suppress their aggregation. As a result, this 3D hybrid anode exhibits high rate performance (1022 mA h g^{-1} at 0.2 A g^{-1} and 270 mA h g^{-1} at 10 A g^{-1}) and extremely long cycling stability (capacity retention > 96% after 1000 cycles) (Fig. 14c–g). More examples of 3DCN-based materials for the anode of LIBs are listed in Table 3. Moreover, the composites combining 1D or 2D nanomaterials with 3DCNs conduct better performance than a single type of materials. In this aspect, a network constructed by carbon nanotubes and 3D carbon nanosheets network can integrate the advantages: (1) the nanosheets supplies large specific surface area; (2) the interconnected CNTs serves as electron conductive paths and reinforces the whole architecture. As a result, this 1D/3D carbon hybrid achieves electrochemical properties used in Li-ion battery for long-run experiments: reversible capacity is 358 mA h g^{-1} after 1000 cycles tested at 2 A g^{-1} (Fig. 14h, i) [104]. Besides, the abovementioned 3D FL-MoS_2@PCNNs materials were tested as the anode of LIBs. Since 3D PCNN ensure the fast transport of both electrons and ions in the whole electrode, the composite of 2D MoS_2 and carbon network achieves a specific capacity as large as 709 mA h g^{-1} delivered at 2 A g^{-1} and maintains ~95.2% even after 520 deep charge/discharge cycles.

Li-S battery is another type of lithium battery, by using sulfur as the cathode. The theoretical capacity of the pure sulfur electrode is 1675 mA h g^{-1} [132]. However, the low electrical conductivity and the instability of sulfur greatly limit its practical application. A facile *in situ* method was reported by Geng's group to prepare 3D porous carbon-containing sulfur NPs (3D S@PGC) with a 90 wt% of sulfur loading [133]. Merited by this high sulfur content and the strong bonding between sulfur and carbon matrix, this 3D S@PGC cathode demonstrates the high specific capacity of 1382 mA h g^{-1} and long cycling stability (0.039% capacity decay at 2 C) (Fig. 15a–e). Moreover, the low-cost ice templates were extended to synthesize sulfur-containing 3D porous carbon by adding sodium poly(4-styrene sulfonate) with carbon source as the starting materials. The following heat treatment at 800 °C enabled the generation of sulfur salts, which can further convert into sulfur in the carbon matrix. Although the capacity of this S-containing 3DCNs is not so high, it exhibits great potential to be the candidate for the cathode of Li-S battery.

Another problem in Li-S batteries is the severe shuttle effect of soluble lithium polysulfide intermediates (LiPS), leading to the rapid capacity decay and low coulombic efficiency. In this regard, a

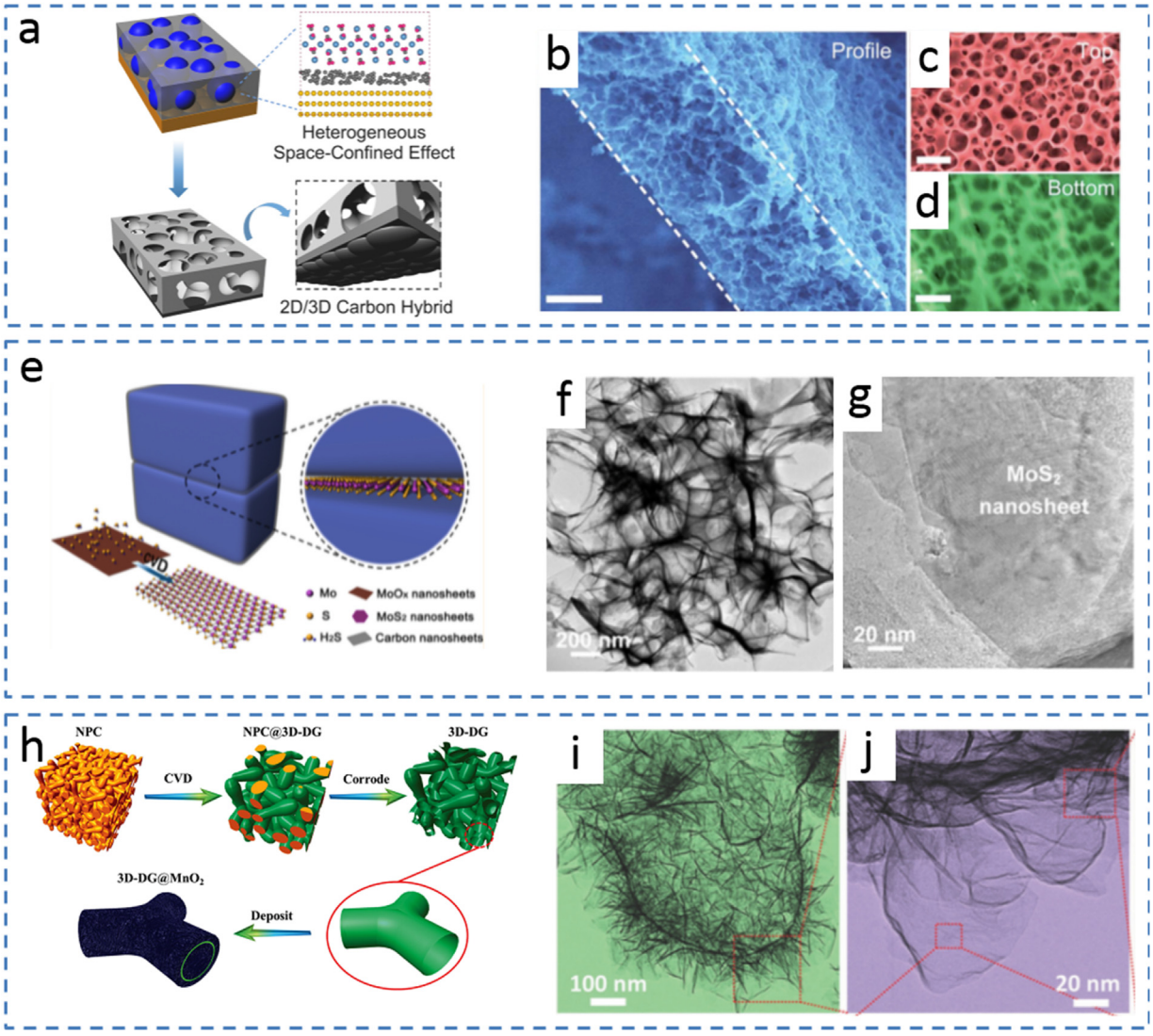

Fig. 13. (a) Schematics of producing N-GPC by salt and metal template. SEM images of (b) profile, (c) top and (d) bottom views of N-GPC film (Reproduced with permission from Ref. [110], Copyright © 2017 Royal Society of Chemistry). (e) Schematics depicting the fabrication procedure and (f, g) TEM images of 3DFL-MoS_2@PCNNs [109]. (h) Schematic of the fabrication process and (i,j) TEM images of the 3D-DG@MnO_2 film (Reproduced with permission from Ref. [38], Copyright © 2016 Wiley-VCH).

Table 3
The battery performance comparison for various nanomaterials and their composites with 3DCNs produced by NaCl template methods.

Battery	Materials	Capacity (mAh g^{-1})	Rate performance (mAh g^{-1})	Long cycle	Ref
LIB	Sn@3DCN	1022 @0.1 A g^{-1}	459 @ 5 A g^{-1}	1000 cycles @ 2 A g^{-1}	[91]
	Sn/C	500 @0.1 A g^{-1}	50 @ 5 A g^{-1}		
	MoS_2@3DCN	1060 @0.1 A g^{-1}	709 @ 2 A g^{-1}	520 cycles @ 2 A g^{-1}	[109]
	MoS_2	600 @0.1 A g^{-1}	50 @ 2 A g^{-1}		
	MoS_2/C	600 @0.1 A g^{-1}	20 @ 2 A g^{-1}		
	SiO_2@3DCN	434 @ 0.1 A g^{-1}			[94]
	Fe_2GeO_4@3DCN	1280 @0.4 A g^{-1}			[92]
	Fe_2GeO_4	400 @ 0.4 A g^{-1}			
	FeS@3DCN	703 @ 1 A g^{-1}	530 @ 5 A g^{-1}		[140]
	FeS	200 @ 1 A g^{-1}			
	$Na_2Ge_4O_9$@3DCN	800 @ 0.2 A g^{-1}		1000 cycles @ 1 A g^{-1}	[141]
	Sb@3DCN	456 @ 0.1 A g^{-1}	270 @ 2 A g^{-1}		[142]
	Sb	10 @ 0.1 A g^{-1}			
SIB	SnSb@3DCN	400 @ 0.1 A g^{-1}	270 @ 2 A g^{-1}	4000 cycles @ 10 A g^{-1}	[90]
	SnSb/N-C	300 @ 0.1 A g^{-1}	200 @ 2 A g^{-1}		
	Fe_2GeO_4@3DCN	350 @ 0.1 A g^{-1}			[92]
	Fe_2GeO_4	250 @ 0.1 A g^{-1}			
	Ni_3S_2@3DCN	600 @ 0.1 A g^{-1}	453 @ 2 A g^{-1}	200 cycles @ 2 A g^{-1}	[143]
	Ni_3S2	250 @ 0.1 A g^{-1}	50 @ 2 A g^{-1}		

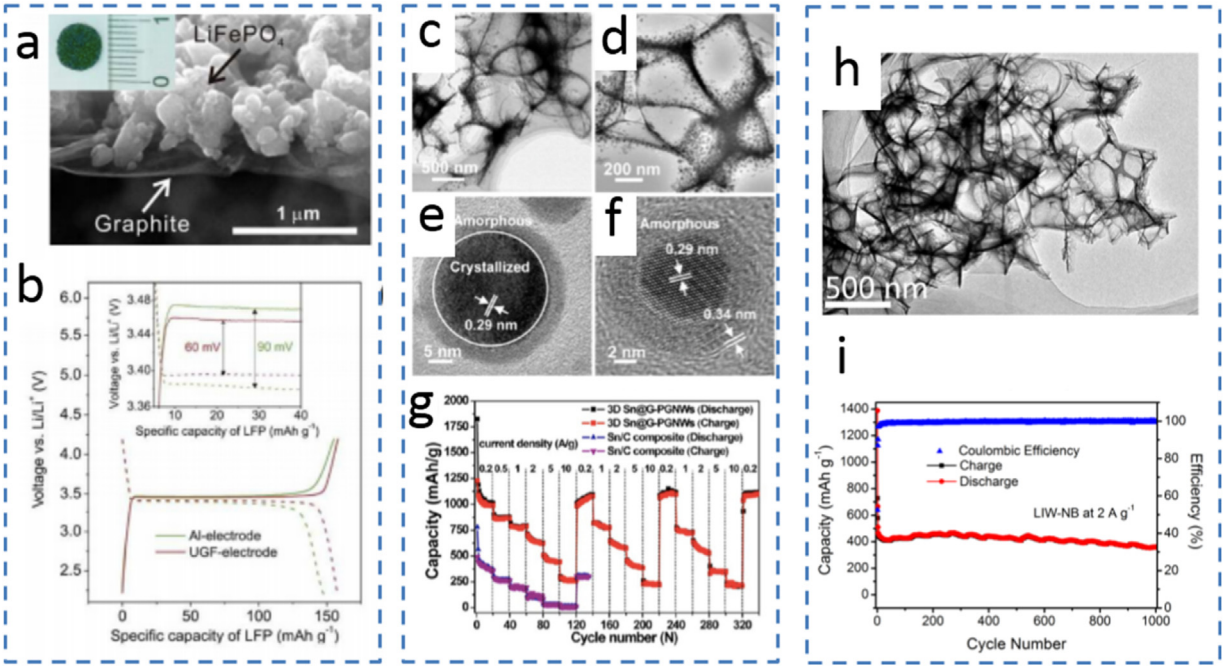

Fig. 14. (a) SEM image and photograph (inset) of the UGF/$LiFePO_4$ (Reproduced with permission from Ref. [128], Copyright © 2012 American Chemical Society). (b) The DC charge/discharge profile of UGF- and Al-electrode. (c,d) TEM images, (e,f) HRTEM images and (g) rate cycle performance of the electrodes at various rates of 3D Sn@G-PGNWs (Reproduced with permission from Ref. [91], Copyright © 2014 American Chemical Society). (h) TEM image and (i) cycle performance and coulombic efficiency of the electrode at 2 A g^{-1} for LIW-NB (Reproduced with permission from Ref. [104], Copyright © 2016 Elsevier).

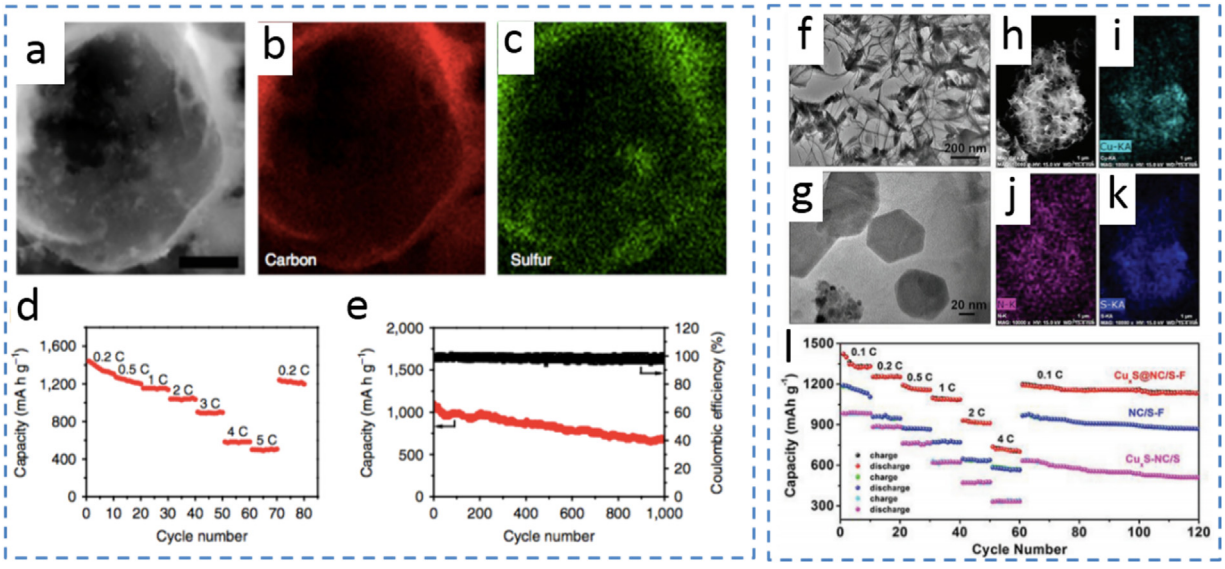

Fig. 15. (a) The TEM image of 3D S@PGC (90% S) composite, and EDS elemental maps of (b) carbon and (c) sulfur (Scale bars: 200 nm) (Reproduced with permission from Ref. [133], Copyright © 2016 Nature Publishing Group). (d) Rate performance and (e) cycling performance of (1000 cycles) of 3D S@PGC. (f) TEM images of Cu@NC-F networks, and (g) TEM image of Cu_xS@NC/S—F composite (Reproduced with permission from Ref. [134], Copyright © 2018 Wiley-VCH). (h, i, j, k) EDS element mapping images of Cu, N, and S, respectively. (l) Rate capability at various current densities of Cu_xS@ NC/S—F, Cu_xS-NC/S, and NC/S—F composite electrode.

3D Cu/N co-doped carbon network was developed by freeze-drying NaCl template method [134]. This 3DCN-based material possesses strong chemical absorption for LiPSs since Cu/N-doping effect serves as the confinement for polysulfides by chemical bonding. Moreover, a further sulfidation process can convert Cu into copper sulfide (Cu_xS), which were still embedded on 3DCNs. When tested in Li-S batteries, this composite shows a high capacity of 1432 mA h g^{-1} with a coulombic efficiency of nearly 100% (Fig. 15f–l). Also, it is effective to enhance the polysulfides adsorption by introducing the second phase in the carbon-based materials. Qiao et al. reported a two-dimensional (2D) heterostructured MoN-VN as a new model sulfur host [135]. Since the electronic structure of MoN can be tailored by incorporation of V, this composite can enhance the polysulfides adsorption and result in the high capacity of 708 mA h g^{-1} with high sulfur loading (3.0 mg cm^{-2}).

Similar to LIB, SIB is a rechargeable battery by transferring sodium ions between the cathode and anode [136,137]. Comparing with lithium, the raw materials for sodium are abundant in reserves and low-cost. Meanwhile, there are some unique requirements for the materials for the SIB electrode. For example, graphite

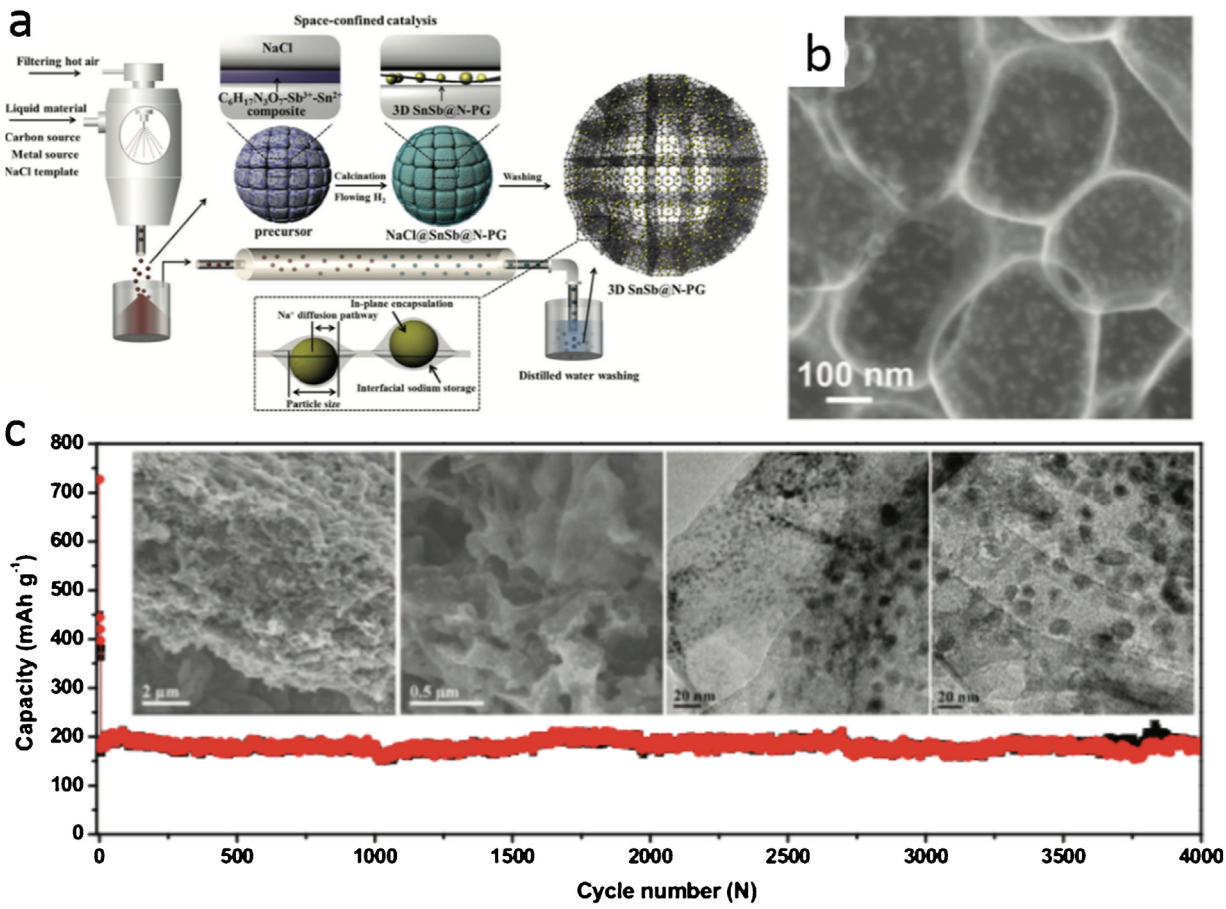

Fig. 16. Schematic illustration of the top-down in situ synthesis of 3D SnSb@N–PG composite. (b) SEM image of the 3D SnSb@N-PG composite. (c) Cycling stability of the 3D SnSb@N–PG electrode at 10 A g^{-1} for 4000 cycles. Insets are SEM and TEM images of the 3D SnSb@N–PG electrode after 4000 cycles (Reproduced with permission from Ref. [90], Copyright © 2018 Wiley-VCH).

performs well in LIB, enjoying the theoretical capacity of 372 mA h g^{-1}. However, the same material has a low sodium storage capacity of 31 mA h g^{-1}. Therefore, searching for suitable materials is crucial for the development of SIBs. For example, red phosphorus is a kind of promising anode material due to its ultrahigh sodium storage capacity (2595 mA h g^{-1}) for SIBs. However, red P has the disadvantages of insulating property and volume variation during cycling, which cause low capacity and unstable cycling performance in practical applications. To deal with these issues, red P was confined in a 3D N-doped microporous carbon matrix (P@N-MPC) by using the ZIF-8 template [138]. As the anode in SIB, this P@N-MPC shows a high reversible specific capacity of 600 mA h g^{-1} at 0.15 A g^{-1} with a low capacity fading rate of 0.02% per cycle. The ultramicropores (< 1 nm) of carbon matrix facilitates the rapid diffusion of electrolyte ions and improves the conductivity of red P. Moreover, N-MPC can relief the volume change of red P during sodiation/desodiation processes, ensuring its long cycle life. Another example of the 3DCNs application in SIBs is the SnSb alloy NPs confined in 3D N-doped porous graphene networks (3D SnSb@N-PG) [90]. This composite (45 wt % of SnSb) shows superior performance, including the high capacity (400 mA h g^{-1}) and cycling stability (190 mA h g^{-1} after 4000 cycles at 10 A g^{-1}) (Fig. 16). Investigate by *in-situ* TEM, the SnSb nanocrystals in composite transform into the hollow structure during charge/discharge processes, indicating that the SnSb are in-plane embedded in graphene and maintain its stability after repeated cycles. At the same time, 3D carbon can be used as a coating layer to improve the overall performance of the electrode. As the anode of sodium-ion batteries, the $Na_2Ti_3O_7$ hollow spheres coated by **N**-doped carbon ultrathin nanosheets shows superior rate performance and achieves 60 mA h g^{-1} after 1000 cycles at 50 C [139]. Such performance is derived from the unique multilayer structure of nanosheets, which reduce the Na-ion diffusion energy consumption and increase electronic conductivity. In addition to regulating the structure of carbon materials, researchers have found that by controlling the inter-spacing of carbon layers can improve its anode performance in the sodium-ion battery. The graphene with controllable layer spacing can achieve 56.6 mA h g^{-1} at the ultrahigh rate of 40 A g^{-1} [121]. Also, the electrode combing with titanium carbide and carbon exhibits the reversible capacities of 72 mA h g^{-1} at 5 A g^{-1} in sodium ion batteries [122].

In order to demonstrate the advantages of 3DCNs in battery-type applications, we summarized the performance of 3DCN-based composite prepared by the same NaCl template. By combining with 3DCNs, various nanomaterials achieved enhanced performance as the electrodes of LIBs and SIBs, including increased capacity, enhanced rate performance and improved cycle stability (Table 3).

Supercapacitors

The supercapacitor is a kind of electrochemical energy storage devices with great potential in the power delivery and energy harvesting applications. According to $E = 0.5CV^2$, the energy density (E) is proportional to the specific capacitance (C) and the square of voltage window (V) [144]. Thus, researchers aim to increase capacitance and expand voltage windows for enhancing the performance of supercapacitors.

To increase the capacitance, two main factors are considered, which are improving the structures (specific surface area and pore

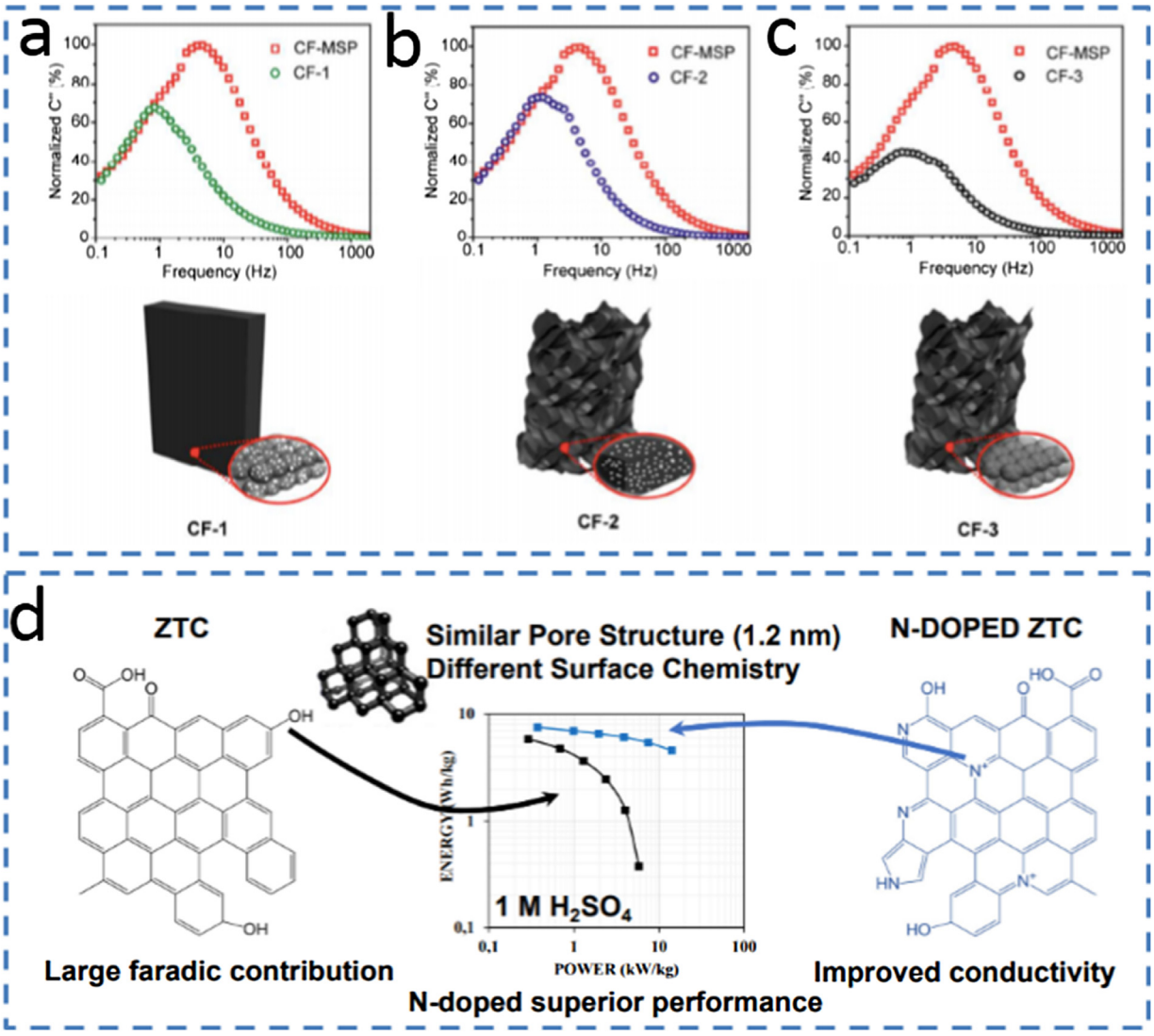

Fig. 17. (a–c) The plot of normalized C″ as a function of frequency and the schematic for the structures for the CF samples with various pore size distributions (Reproduced with permission from Ref. [147], Copyright © 2017 American Chemical Society). (d) The comparison between ZTC and N-ZTC (Reproduced with permission from Ref. [148], Copyright © 2018 Elsevier).

size distribution) and introducing heteroatoms in carbon matrix [145,146]. Since the electric double layer is a surface phenomenon, a larger surface area is required to achieve high capacitance. We demonstrate that controlling the types and ratio of the salt template can adjust the morphology of 3DCNs, and directly influence the capacitance. By mixing three types of NaX salts, the obtained 3D porous carbon network delivered a capacitance of 320 F g^{-1} at 0.5 A g^{-1} due to its high specific surface area (1088 m^2 g^{-1}) [18]. By comparison, the carbon sample fabricated by single NaCl template only shows 147 F g^{-1} at 0.5 A g^{-1}, because of its lower specific surface area of 608 m^2 g^{-1}. Secondly, to reveal the different roles of pores, Lu's group adopted the silica template and chemical etching method to produce the carbon matrix with multi-scale pores [147]. In their work, this porous carbon (CF) electrode achieves a remarkable capacitance of 375 F g^{-1} at the current density of 1 A g^{-1}. Even at the ultrahigh current density of 500 A g^{-1}, the electrode still remains 236 F g^{-1}. This remarkable capacitive property derives from the large surface area of 2905 m^2 g^{-1}, which enables an 88% of charge are stored by the electrical double layer. Moreover, the hierarchical porous structure allows efficient ion diffusion and charge transfer, resulting in the excellent rate capability (Fig. 17a–c).

Besides the morphology, the components also affect the capacitive properties of 3DCNs. To this regard, two kinds of ZTCs were produced to investigate the influences of N-doping effect [148]. Both of these samples have a comparable structure yet different surface functional groups: the N-ZTC has 4 at% N-doping in a carbon matrix, and most of them are quaternary N (N–Q). Tested in 1 M H_2SO_4, the N-ZTC electrode achieves higher energy density (6.7 Wh kg^{-1}) than ZTC (5.9 Wh kg^{-1}). Meanwhile, the power density (98 kW kg^{-1}) of N-ZTC electrode is four times higher than the value of ZTC, since the electrical conductivity was enhanced by the N–Q functionalities in N-ZTC (Fig. 17d). Coordinating the above two aspects, the optimized template method for preparing 3DCNs show superior comprehensive performances. Zhao et al. reported a facial self-template strategy to produce 3D the mesoporous carbon nanofibers using ethylene glycol as the carbon precursor and $Zn(CH_3COO)_2$ as the structural constructor. The mesoporous carbon production prepared by this self-template method has a high surface area of 1725 m^2 g^{-1}, and rich oxygen surface functionalities (9 wt%). As a result, these carbon materials show high capacitance in both aqueous (280 F g^{-1}) and organic electrolytes (168 F g^{-1}) [149]. Huang's group reported that an **N**-doped ordered mesoporous few-

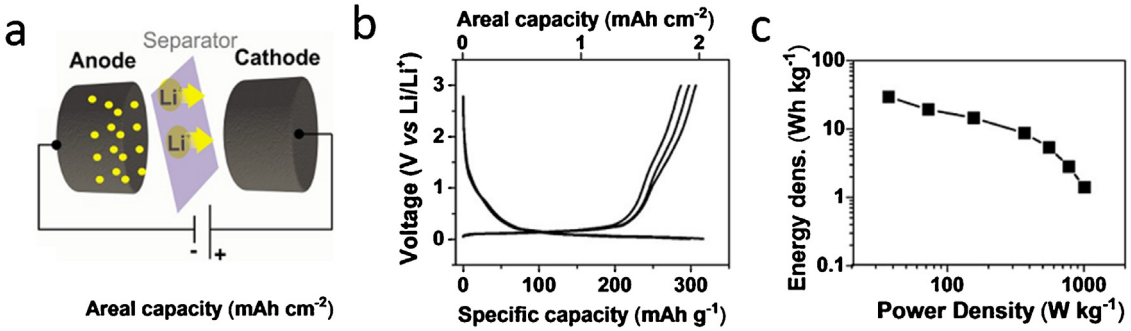

Fig. 18. (a) Scheme of LIC, (b) Galvanostatic charge-discharge curve at 0.1 A g^{-1} and (c) Ragone plot of the 3D rebar GF (Reproduced with permission from Ref. [107], Copyright © 2017 American Chemical Society).

layer carbon (OMFLC) were synthesized by the mesoporous silica template [150]. This 3D porous carbon can achieve a capacitance as high as 855 F g^{-1} in aqueous electrolytes since N-associated defects in graphene-like layered carbon caused the robust redox reactions. In addition, this mesoporous carbon network was able to store a specific energy of 41 Wh kg^{-1} in an electrochemical cell.

To expand the operation voltage of supercapacitors, one effective strategy is to choose electrolyte with high decomposition voltages, such as organic electrolyte and ionic liquids [28]. To cooperate with these novel electrolytes, Hu et al. combined porous Cu and MgO templates to synthesize 3D hierarchical carbon nanomaterials [151]. The obtained 3D few-layer graphene-like carbon (3DG) has a large specific surface area (1500 m^2 g^{-1}) and high conductivity (800 S m^{-1}). Moreover, this carbon material exhibits high wettability in ionic liquid electrolytes. As a result, this 3DG presented a wide voltage window of 4 V in the electrolyte of $EMIMBF_4$, whose maximum power density was 740.8 kW kg^{-1}. Another effective method to extend the voltage window is to assemble asymmetric supercapacitors (ASCs). Qin et al. synthesized a free-standing 3D duct-like graphene (3D-DG) by porous metal template, which acts as the robustness backbone for depositing MnO_2 nanosheets (3D-DG@MnO_2) [38]. To assembly ASC, 3D-DG@MnO_2 acted as the positive electrode and 3D-DG served as the negative electrode. This device displayed ultrahigh volumetric energy density (28.2 mW h cm^{-3}) and power density (55.7 W cm^{-3}) at 2.0 V in $LiNO_3$-PVA gel electrolyte (Fig. 18a–c). Furthermore, a piece of this kind of ACS can illuminate 25 LED lamps at the same time, supporting its high energy density and promising application prospect [38].

Noteworthy, the use of lithium-ion in the capacitor also resulted in high energy density. The lithium-ion capacitors (LIC) capture the merits of the electric double-layer capacitor (EDLCs) and LIBs: its positive electrode utilizes the materials for EDLCs, and the negative electrode material uses the material for LIBs [152,153]. Tested as electrodes of a LIC, the 3D rebar GF made by Ni powder template achieved the capacity of 320 mA h g^{-1} and the energy density as high as 32 Wh kg^{-1} (Fig. 18a–c) [107].

By investigating the electrochemical performance of 3DCN-based batteries and supercapacitors, we can summarize the advantages of 3DCN in electrochemical applications into two aspects, including the three-dimensional morphology and the porous structure. The 3D structure mainly plays its function in the electrode condition with high mass-loading. [154]. With gradual increasing the mass of the active material, it will affect the mass-transfer and charge-transfer process in the whole electrode. In addition, for the electrode with larger thickness, only a part of the surface active material can give full play to the electrochemical performance. In such a system, the electrode based on 3DCN active material can show its advantages in order to ensure efficient material transfer and charge transfer (Fig. 19a). Therefore, 3DCN-based electrodes are particularly suitable for energy storage applications with high capacity and high rate. For example, the 3D electrodes composed Nb_2O_5 and 3D graphene (Nb_2O_5/HGF-2.0) exhibits the similar capacity with the mass loading increasing. In contrast, the capacity of a simple mixture of Nb_2O_5 and graphene decrease rapidly (Fig. 19b, c). According to the voltage-capacity curves of these two types of electrodes, Nb_2O_5/HGF-2.0 has the lower voltage drops than Nb_2O_5/graphene electrode. On the other hand, the pores introduced by 3D structure can contribute to ion transportation greatly. The tailored pores in a 3D holey graphene framework (HGF) electrode can serve as the shortcuts for the rapid ion diffusion (Fig. 19d, e). The electrochemical impedance spectroscopy tests (Fig. 19f, g) demonstrate that HGF electrodes have the advantage of smaller equivalent series resistance (0.65 Ω) and shorter time constant (0.17 s).

Fuel cells

As a promising energy conversion application, a fuel cell converts chemical energy into electrical energy by reducing oxygen gas at the cathode and oxidizing fuel (e.g., H_2 gas) at the anode [155,156]. In the practical devices, the oxygen reduction reaction (ORR) at the cathode plays the key role in improving the performance of a fuel cell device, since the four-electron transfer process of ORRs is sluggish [157,158]. Fuel cells with noble metal loaded carbon were developed for catalyzing ORR reactions [159]. However, since non-porous carbon has sluggish dynamics in reaction and has low charge/discharge round-trip efficiency [160,161], 3D porous carbon combined with highly efficient catalysts are attracted research interest and, which can achieve improved performance. Sun et al. fabricated 3D graphene decorated by Ru nanocrystals. As the cathode for Li-O_2 batteries, this Ru/carbon composite can operate reversibly with high capacity and good stability [160].

Yet, the high cost of noble metal (Pt, Ru) greatly obstructs their commercial applications. Recently, researchers investigated many kinds of alternative ORR catalysts with high activity and low cost, such as heteroatom-doping carbon, non-precious metal, and metal oxides [161–164]. In these aspects, 3DCNs and their composites derived from hard templates have attracted great attention due to their controllable structure and high electron conductivity. For example, a 3D N-doped hierarchical porous carbon monolith (NHPCM) was synthesized by an *in situ* source-template-interface reactions (Fig. 20a–d). This material composed by branched mesoporous rods, which is derived from the nanocasting of N-doped hierarchical porous silica monolith (NHPSM) [165]. In the process, NHPSM not only acts as a hard template but also provides N atoms for the doping effect. The N-doping can attribute to the solid-solid interface reactions of carbon source and N functional groups inside the nanospaces of the hard template (Fig. 20e–h). As a result, these

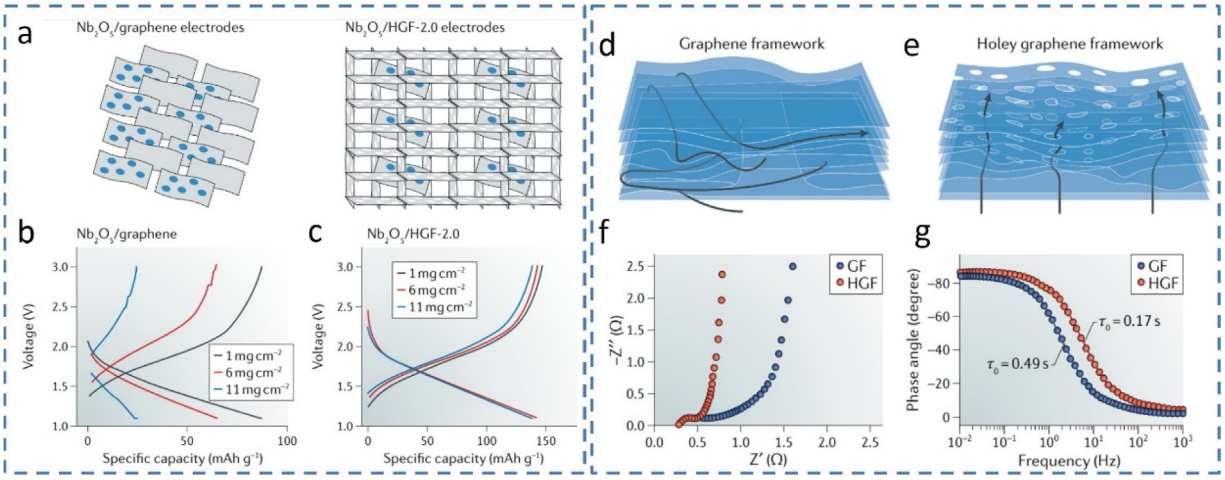

Fig. 19. (a) Schematics comparing the structures of the 2D and 3D porous composite electrode. (b) Galvanostatic charge/discharge curve for the 2D Nb_2O_5/graphene electrodes with different mass loading. (c) Galvanostatic charge/discharge curve for the Nb_2O_5/HGF-2.0 electrode with different mass loading. (d) Illustration of a compressed film of graphene (e) Illustration of a holey graphene framework (HGF) with arrows depicting the ion transport pathways. (f) Nyquist plots and (g) Bode plots of GF and HGF electrodes in 6 M KOH (Reproduced with permission from Ref. [154], Copyright © 2018 Nature Publishing Group).

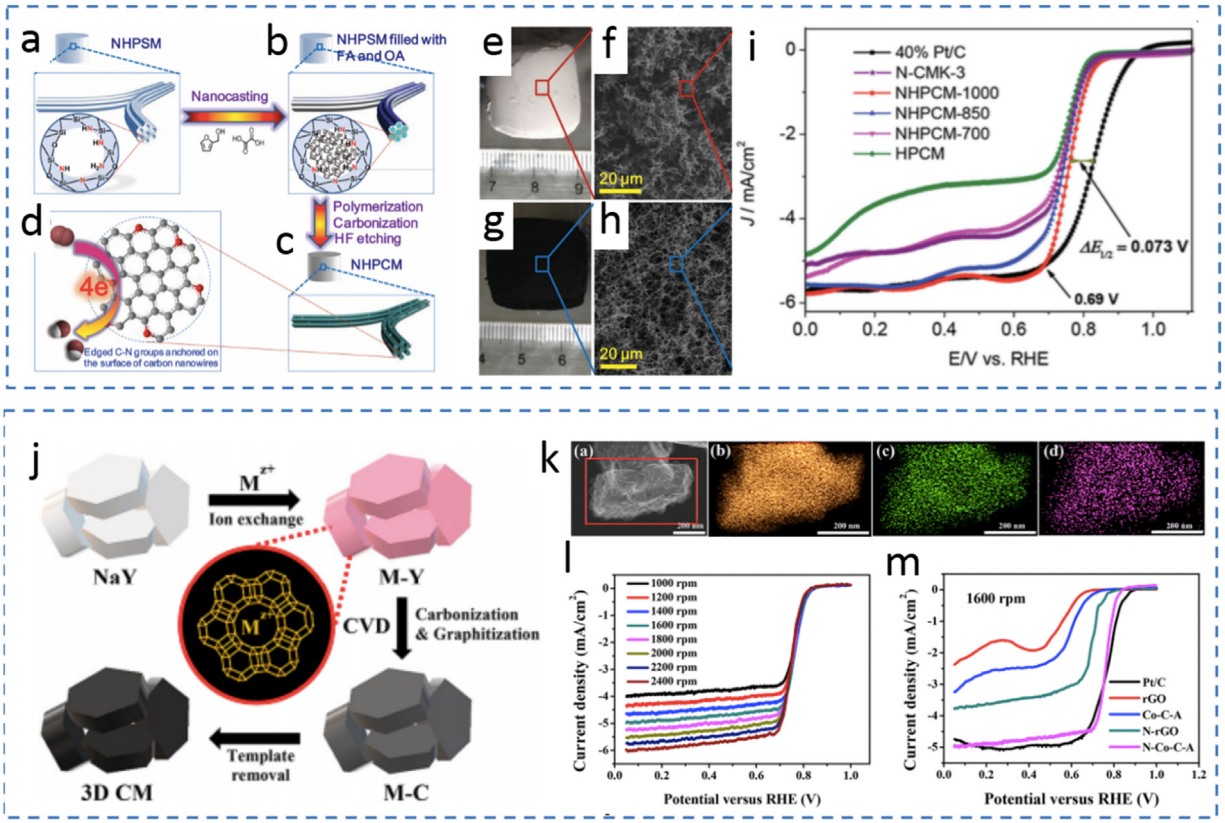

Fig. 20. (a–c) A nanocasting strategy to synthesize NHPCM using NHPSM as both a hard template and N source. (d) The four-electron ORR process catalyzed by edged C–N groups anchored on the surface of NHPCM. (e) The digital photos and (f) cross-sectional SEM of NHPSM. (g) The digital photos and (h) cross-sectional SEM of NHPCM. (i) LSV curves of different samples in O_2-saturated 0.1 M KOH at 1600 rpm (5 mV s^{-1}) (Reproduced with permission from Ref. [165], Copyright © 2015 Wiley-VCH). (*j*) Schematic for the fabrication of 3D carbon materials (3D CMs) by using Zeolite Y as a hard template. (k) STEM image and EDX mapping for carbon (orange), nitrogen (green), and cobalt (purple) elements. (l) LSV curves of N-Co-C-A with different rotating speed. (m) LSV curves of different samples at 1600 rpm with a scan rate of 10 mV s^{-1} (Reproduced with permission from Ref. [166], Copyright © 2018 American Chemical Society).

edged C–N functional groups on the surface of the carbon matrix presents superior electrocatalytic activity in a four-electron dominant reaction pathway. By conducting linear sweep voltammetry (LSV) in O_2-saturated 0.1 M KOH, NHPCM shows a positive shift of the onset potential (0.88 V vs RHE) comparing to N-free sample (0.82 V), which is still higher than the commercial Pt/C (Fig. 20i). The enhanced performance of ORR derives from the increased exposure of the catalytic sites since the O_2 could be more favorably activated at the edged groups than in the basal planes.

Another strategy for developing a high-efficient ORR catalyst is to incorporate non-precious metal or metal oxides into the 3DCNs. As a typical example, Xu et al. synthesized Fe/N-doped graphic porous carbon (Fe/N-GPC) by using the nanospaces of MOFs to encapsulate metal nanoparticles precursors. Fe/N-GPC exhibits a

half-wave potential of -0.13 V versus Ag/AgCl [68]. A series of 3D microporous carbon materials with high specific surface areas and large pore volumes were prepared by using transition metal ion-exchanged zeolites as a hard template [166]. In this method, *in situ* incorporation of transition metal atoms inside 3D carbon materials (3D CM) was achieved, and the amount of the metal can be tuned by a post selective leaching (Fig. 20j,k). In this class of materials, the N-doped cobalt-carbon sample (N-Co-C-A) shows an onset potential comparable to a commercial Pt/C (20 wt %) (Fig. 20l, m). Comparing with CNTs and graphene, this 3DCN-based catalyst exhibits good durability and superior activity in ORR. The improved performance of N-Co-C-A derives from the well-defined pore distribution stemming from the 3D structure, which facilitates the electrolyte and O_2 diffusion and enhances the contact between the active sites and electrolyte.

Along with 3D N-doped carbon networks prepared by MOF and zeolite templates, salt-template synthesized N-doped 3DCNs have also been demonstrated to show good ORR electrocatalytic activities. As an example, an edge-rich N-doping porous carbon with a high proportion of pyridinic and pyrrolic N (94%) was synthesized by using nano $CaCO_3$ as template [167]. The obtained samples exhibit 3D structure, hierarchical pores, and large pore volumes and a large number of active sites for catalyzing ORR. As a result, the sample shows the half-wave potential of 0.853 V and long-term stability in alkaline media, which is among the best in similar metal-free catalysts.

The reaction rate and stability of ORR can be further improved by introducing two kinds of heteroatoms in 3DCN. A 3D nanoporous graphene synthesized by nanoporous Ni template, then this 3D graphene can be doped with both N and Ni single atoms/clusters. The pre-doping of N is in favor of increasing the Ni doping amount. The resulting N and Ni co-doped 3D graphene have excellent electrocatalytic activities for ORR in 0.1 M KOH [168]. Zhao et al. reported submillimeter-scaled carbon networks decorated with single atoms by MOF-template. Zn-based MOFs doped with Co and Fe ions were used as precursors. The consequent pyrolysis process enabled organics decomposed to form the hierarchically pores and formed the metal ions (Fe and Co). The as-obtained product (CoFe@C) exhibits superior electrocatalytic in the alkaline electrolyte, which shows more positive onset potential and half-wave potential than those of commercial Pt/C [169].

Summary and outlook

In this review, we have summarized the recent development on the hard-templated synthesis of 3DCNs and their composites, and the application of 3DCNs-based materials in fields of energy storage and conversion. Merited by hard template strategy, researchers were able to controllably synthesize 3DCNs in the aspects of structures, properties, and processes to meet the demand of applications. Firstly, it is achievable to tune the structure of 3DCNs from microscopic to the macroscopic scale, including the specific surface area, pore volume, and pore size distribution. The sub-structures of the 3DCNs transform from 0D (nanopowder or NPs), to 1D (nanowires or nanotube), and 2D (nanosheets or nanoplate) as well. Secondly, the physical and chemical properties of 3DCNs, including chemical conductivity, thermal conductivity, mechanical stability, etc., can be adjusted by combining with other nanomaterials. Thirdly, the mechanical properties of the 3DCNs can be strengthened by shifting the pore size and combining with reinforcements. Fourthly, the production processes of 3DCNs have the potential for industrial production by using simple and low-cost hard templates, such as water-soluble salt template and ice template.

To achieve these virtues, there are several important factors should be considered in the production of 3DCN-based materials by hard templates: (1) selecting the appropriate templates with suitable morphology and pore size; (2) rational coordinating the precursors and the hard templates; (3) choosing appropriate carbonization conditions, such as temperature and atmosphere; (4) adapting the prepared materials to the appropriate applications. Based on these factors, the hard template approach exhibits controllability, versatility, and great potential in the fabrication of 3DCN-based nanomaterials with large specific surface area and porosity, high mass-transfer ability and superior electrical conductivity for efficient energy storage, conversion, and other engineering applications.

Furthermore, there are still several challenges remained to be addressed in materials preparation. Firstly, the morphology of 3DCN-based nanomaterial is difficult to precise control by the template method. Although the hard-templated lithography can solve this problem at the expense of low yield and trivial processes, the 3DCNs with ordered and uniform structure is still rare to obtain. Secondly, the hard-templated 3DCNs suffer from the issues of high production cost. This problem is especially critical in the metal and silica template, which involve the tidy preparation process and complex raw materials. Thirdly, all template-based methods inevitably involve the corrosive solution for removing the templates. These processes are often harmful to the environment. How to reduce the waste and pollution in such processes is an important step to play the potential of template method. To this regard, water-soluble salts have certain advantages, since they can be removed and recycled by simple water washing. Sustained and dedicated researchers still devote to developing low-cost processes to produce high-performance 3DCNs and their composites.

In energy storage application, 3DCN produced by hard templates still have some bottlenecks to overcome. At first, the transport characteristics of ions in 3D configuration materials need to be in-depth studied. Most of the research on ion diffusion is based on the traditional 2D configuration or 1D configuration. To tackle with 3D configuration, it is necessary to combine *in-situ* characterization (i.e. electrochemical scanning electron microscopy) with the construction of new analysis models. Besides, most of 3DCNs face the problem of low density because of its high porosity, which will cause low volume energy density and low volume power density, thus limiting its application potential in some miniaturized equipment. According to this, consideration can be given to further filling the second phase in the pores of 3DCN to increase the overall density of the material. By overcoming abovementioned issues, we believe that hard-template derived 3DCN-based materials will provide us with great potential for the state-of-art applications in the fields of energy, environment, and medicine, *etc.*

Notes

The authors declare no competing financial interest.

Acknowledgment

The authors gratefully acknowledge the financial support by the National Natural Science Foundation of China (Grant No. 51531004, 51771130 and 51801135), the Tianjin youth talent support program, the Tianjin Natural Science Funds for Distinguished Young (Grant No. 17JCJQJC44300), the Tianjin Science and Technology Support Project (Grant No. 17ZXCLGX00060), and the Independent Innovation Fund of Tianjin University (1805).

References

[1] X. Cao, Z. Yin, H. Zhang, Energy Environ. Sci. 7 (2014) 1850–1865.
[2] D.R. Rolison, J.W. Long, J.C. Lytle, A.E. Fischer, C.P. Rhodes, T.M. McEvoy, et al., Chem. Soc. Rev. 38 (2009) 226–252.

[3] C. Zhu, T. Liu, F. Qian, W. Chen, S. Chandrasekaran, B. Yao, Y. Li, et al., Nano Today 15 (2017) 107–120.
[4] A. Ghosh, Y.H. Lee, ChemSusChem 5 (2012) 480–499.
[5] Y.P. Zhai, Y.Q. Dou, D.Y. Zhao, P.F. Fulvio, R.T. Mayes, S. Dai, Adv. Mater. 23 (2011) 4828–4850.
[6] Y. He, X. Zhuang, C. Lei, L. Lei, Y. Hou, Y. Mai, et al., Nano Today 24 (2019) 103–119.
[7] H. Jiang, P.S. Lee, C.Z. Li, Energy Environ. Sci. 6 (2013) 41–53.
[8] A. Dasgupta, L.P. Rajukumar, C. Rotella, Y. Lei, M. Terrones, Nano Today 12 (2017) 116–135.
[9] A.H. Lu, F. Schueth, Adv. Mater. 18 (2006) 1793–1805.
[10] C. Liang, Z. Li, S. Dai, Angew. Chem. Int. Ed. 47 (2008) 3696–3717.
[11] V. Malgras, J. Tang, J. Wang, J. Kim, N.L. Torad, S. Dutta, et al., J. Nanosci. Nanotechnol. 19 (2019) 3673–3685.
[12] X.W. Lou, L.A. Archer, Z. Yang, Adv. Mater. 20 (2008) 3987–4019.
[13] B. Jache, C. Neumann, J. Becker, B.M. Smarsly, P. Adelhelm, J. Mater. Chem. 22 (2012) 10787–10794.
[14] F. Cheng, Z. Tao, J. Liang, J. Chen, Chem. Mater. 20 (2008) 667–681.
[15] H. Nishihara, T. Kyotani, Adv. Mater. 24 (2012) 4473–4498.
[16] T. Kyotani, N. Sonobe, A. Tomita, Nature 331 (1988) 331–333.
[17] K.Q. Qin, J.L. Kang, J.J. Li, C.S. Shi, Y.X. Li, Z.J. Qiao, et al., ACS Nano 9 (2015) 481–487.
[18] S. Zhu, J.J. Li, C.N. He, N.Q. Zhao, E.Z. Liu, C.S. Shi, et al., J. Mater. Chem. A 3 (2015) 22266–22273.
[19] S.N. Schiffres, S. Harish, S. Maruyama, J. Shiomi, J.A. Malen, ACS Nano 7 (2013) 11183–11189.
[20] A.B. Fuertes, G. Lota, T.A. Centeno, E. Frackowiak, Electrochim. Acta 50 (2005) 2799–2805.
[21] A.J. Amali, J.K. Sun, Q. Xu, Chem. Commun. 50 (2014) 1519–1522.
[22] J. Banhart, Prog. Mater. Sci. 46 (2001) 559–632.
[23] H.J. Xu, Z.B. Xing, F.Q. Wang, Z.M. Cheng, Chem. Eng. Sci. 195 (2018) 462–483.
[24] W. Zhu, R. Zhang, F. Qu, A.M. Asiri, X. Sun, ChemCatChem 9 (2017) 1721–1743.
[25] Z. Chen, W. Ren, L. Gao, B. Liu, S. Pei, H.M. Cheng, Nat. Mater. 10 (2011) 424–428.
[26] H. Sun, Y. Liu, Y. Yu, M. Ahmad, D. Nan, J. Zhu, Electrochim. Acta 118 (2014) 1–9.
[27] Q. Meng, K. Qin, L. Ma, C. He, E. Liu, F. He, et al., ACS Appl. Mater. Interfaces 9 (2017) 30832–30839.
[28] Y. Ito, Y. Tanabe, H.J. Qiu, K. Sugawara, S. Heguri, N.H. Tu, et al., Angew. Chem. Int. Ed. 53 (2014) 4822–4826.
[29] Y. Xue, D. Yu, L. Dai, R. Wang, D. Li, A. Roy, et al., Phys. Chem. Chem. Phys. 15 (2013) 12220–12226.
[30] Q. Chen, Y. Ding, M. Chen, MRS Bull. 43 (2018) 43–48.
[31] Z. Lu, C. Li, J. Han, F. Zhang, P. Liu, H. Wang, et al., Nat. Commun. 9 (2018) 276.
[32] L. Lührs, J. Weissmüller, Scr, Mater. 155 (2018) 119–123.
[33] Z. Li, H. Bian, C.M. Lee, X. Chen, Y.Y. Li, Thin Solid Films 65 (2018) 1–6.
[34] N.T. Nguyen, S. Ozkan, O. Tomanec, X. Zhou, R. Zboril, P. Schmuki, J. Mater. Chem. A 6 (2018) 13599–13606.
[35] M. Hakamada, M. Mabuchi, J. Alloy Comp. 485 (2009) 583–587.
[36] E. Detsi, J.B. Cook, B.K. Lesel, C.L. Turner, Y.L. Liang, S. Robbennolt, et al., Energy Environ. Sci. 9 (2016) 540–549.
[37] T. Aburada, J.M. Fitz-Gerald, J.R. Scully, Corros. Sci. 53 (2011) 1627–1632.
[38] K. Qin, E. Liu, J. Li, J. Kang, C. Shi, C. He, et al.,Adv. Energy Mater. 6 (2016), 1600755.
[39] L. Wang, K. Qin, J. Li, N. Zhao, C. Shi, L. Ma, et al., Appl. Surf. Sci. 427 (2018) 598–604.
[40] J. Sha, C. Gao, S.K. Lee, Y. Li, N. Zhao, J.M. Tour, ACS Nano 10 (2015) 1411–1416.
[41] S. Drieschner, M. Weber, J. Wohlketzetter, J. Vieten, E. Makrygiannis, B.M. Blaschke, et al., 2D Mater. 3 (2016) 045013.
[42] J. Sha, Y. Li, R. Villegas Salvatierra, T. Wang, P. Dong, Y. Ji, et al., ACS Nano 11 (2017) 6860–6867.
[43] D. Qiu, T. Cao, J. Zhang, S.W. Zhang, D. Zheng, H. Wu, et al., J. Energy Chem. 31 (2019) 101–106.
[44] S. Zhu, J. Li, L. Ma, L. Guo, Q. Li, C. He, et al., ACS Appl. Mater. Interfaces 8 (2016) 11720–11728.
[45] J. Pampel, T.P. Fellinger,Adv. Energy Mater. 6 (2016), 1502389.
[46] M. Li, F. Xu, H. Li, Y. Wang, Catal. Sci. Technol. 6 (2016) 3670–3693.
[47] W. Yang, L. Chen, X. Liu, X. Yue, C. Liu, J. Jia, J. Mater. Chem. A 4 (2016) 5834–5838.
[48] L. Wang, Q. Zhu, J. Zhao, Y. Guan, J. Liu, Z. An, et al., Microporous Mesoporous Mater. 279 (2019) 439–445.
[49] S. Inagaki, T. Nakao, T. Miki, N. Kuroda, Y. Kubota, Microporous Mesoporous Mater. 241 (2017) 123–131.
[50] R.A.L. Sobrinho, G.R.S. Andrade, L.P. Costa, M.J.B. de Souza, A.M.G.P. de Souza, I.F. Gimenez, J. Hazard. Mater. 362 (2019) 53–61.
[51] V. Duraisamy, K. Selvakumar, R. Krishnan, S.M.S. Kumar, ChemistrySelect 4 (2019) 2463–2474.
[52] F.L. Meng, Z.L. Wang, H.X. Zhong, J. Wang, J.M. Yan, X.B. Zhang, Adv. Mater. 28 (2016) 7948–7955.
[53] S. Ungureanu, M. Birot, H. Deleuze, V. Schmitt, N. Mano, R. Backov, Carbon 91 (2015) 311–320.
[54] P.K. Tripathi, L. Gan, M. Liu, N.N. Rao, J. Nanosci. Nanotechnol. 14 (2014) 1823–1837.
[55] J. Schuster, G. He, B. Mandlmeier, T. Yim, K.T. Lee, T. Bein, et al., Angew. Chem. Int. Ed. 51 (2012) 3591–3595.
[56] X. Zuo, X. Wang, Y. Xia, S. Yin, Q. Ji, Z. Yang, et al., J. Power Sources 412 (2019) 93–104.
[57] X. Huang, K. Qian, J. Yang, J. Zhang, L. Li, C. Yu, D. Zhao, Adv. Mater. 24 (2012) 4419–4423.
[58] N. Brun, S.R.S. Prabaharan, M. Morcrette, C. Sanchez, G. Pecastaings, A. Derre, et al., Adv. Funct. Mater. 19 (2009) 3136–3145.
[59] K. Kim, Y. Kwon, T. Lee, S.J. Cho, R. Ryoo, Carbon 118 (2017) 517–523.
[60] H. Noh, S. Choi, H.G. Kim, M. Choi, H.T. Kim, ChemElectroChem 6 (2019) 558–565.
[61] F. Su, X. Zhao, L. Lv, Z. Zhou, Carbon 42 (2004) 2821–2831.
[62] H. Nishihara, Q.H. Yang, P.X. Hou, M. Unno, S. Yamauchi, R. Saito, et al., Carbon 47 (2009) 1220–1230.
[63] K. Nueangnoraj, H. Nishihara, K. Imai, H. Itoi, T. Ishii, M. Kiguchi, et al., Carbon 62 (2013) 455–464.
[64] K. Kim, T. Lee, Y. Kwon, Y. Seo, J. Song, J.K. Park, et al., Nature 535 (2016) 131–135.
[65] W. Li, J. Liu, D.Y. Zhao, Nat. Rev. Mater. 1 (2016) 16023.
[66] Z. Liang, R. Zhao, T. Qiu, R. Zou, Q. Xu,EnergyChem 1 (2019), 100001.
[67] D. Song, Q.L. Zhu, Q. Xu, Nat. Rev. Mater. 3 (2018) 17075.
[68] C.C. Hou, Q. Xu,Adv. Energy Mater. 9 (2019), 1801307.
[69] B. Liu, H. Shioyama, T. Akita, Q. Xu, J. Am. Chem. Soc. 130 (2008) 5390–5391.
[70] W. Chaikittisilp, K. Ariga, Y. Yamauchi, J. Mater. Chem. A 1 (2013) 14–19.
[71] K. Xi, S. Cao, X. Peng, C. Ducati, R.V. Kumar, A.K. Cheetham, Chem. Commun. 49 (2013) 2192–2194.
[72] L. Radhakrishnan, J. Reboul, S. Furukawa, P. Srinivasu, S. Kitagawa, Y. Yamauchi, Chem. Mater. 23 (2011) 1225–1231.
[73] N.L. Torad, M. Hu, Y. Kamachi, K. Takai, M. Imura, M. Naito, et al., Chem. Commun. 49 (2013) 2521–2523.
[74] B. Liu, H. Shioyama, H. Jiang, X. Zhang, Q. Xu, Carbon 48 (2010) 456–463.
[75] L. Zou, C.C. Hou, Z. Liu, H. Pang, Q. Xu, J. Am. Chem. Soc. 140 (2018) 15393–15401.
[76] W. Chen, Y.X. Huang, D.B. Li, H.Q. Yu, L. Yan, RSC Adv. 4 (2014) 21619–21624.
[77] Y.S. Hu, P. Adelhelm, B.M. Smarsly, S. Hore, M. Antonietti, J. Maier, Adv. Funct. Mater. 17 (2007) 1873–1878.
[78] A.D. Roberts, X. Li, H. Zhang, Chem. Soc. Rev. 43 (2014) 4341–4356.
[79] J. Kuang, L. Liu, Y. Gao, D. Zhou, Z. Chen, B. Han, et al., Nanoscale 5 (2013) 12171–12177.
[80] L. Estevez, A. Kelarakis, Q. Gong, E.H. Da'as, E.P. Giannelis, J. Am. Chem. Soc. 133 (2011) 6122–6125.
[81] X. Li, W. Cai, L. Colombo, R.S. Ruoff, Nano Lett. 9 (2009) 4268–4272.
[82] S. Zhu, P.-L. Taberna, N. Zhao, P. Simon, Electrochem. Commun. 96 (2018) 6–10.
[83] Z. Ma, T. Kyotani, A. Tomita, Carbon 40 (2002) 2367–2374.
[84] X.H. Cao, Y.M. Shi, W.H. Shi, G. Lu, X. Huang, Q.Y. Yan, et al., Small 7 (2011) 3163–3168.
[85] J.N. Wang, L. Zhang, J.J. Niu, F. Yu, Z.M. Sheng, Y.Z. Zhao, et al., Chem. Mater. 19 (2007) 453–459.
[86] D.S. Yuan, J. Zeng, J. Chen, Y. Liu, Int. J. Electrochem. Sci. 4 (2009) 562–570.
[87] S. Stankovich, D.A. Dikin, G.H. Dommett, K.M. Kohlhaas, E.J. Zimney, E.A. Stach, et al., Nature 442 (2006) 282–286.
[88] A. Idowu, B. Boesl, A. Agarwal, Carbon 135 (2018) 52–71.
[89] N. Kurra, Q. Jiang, P. Nayak, H.N. Alshareef, Nano Today 24 (2019) 81–102.
[90] J. Qin, T. Wang, D. Liu, E. Liu, N. Zhao, C. Shi, et al.,Adv. Mater. 30 (2018), 1704670.
[91] J. Qin, C. He, N. Zhao, Z. Wang, C. Shi, E.Z. Liu, et al., ACS Nano 8 (2014) 1728–1738.
[92] J. Han, J. Qin, L. Guo, K. Qin, N. Zhao, C. Shi, et al., Appl. Surf. Sci. 427 (2018) 670–679.
[93] S. Zhu, B. Pu, S. Sui, R. Zhang, S. Xu, C. Ma, et al., Mater. Lett. 189 (2017) 236–239.
[94] Z. Yuan, N. Zhao, C. Shi, E. Liu, C. He, F. He, Chem. Phys. Lett. 651 (2016) 19–23.
[95] J. He, Y. Chen, A. Manthiram, iScience 4 (2018) 36–43.
[96] C.H. Choi, M. Kim, H.C. Kwon, S.J. Cho, S. Yun, H.-T. Kim, et al., Nat. Commun. 7 (2016) 10922.
[97] J. Shao, X. Xiao, X. Fan, X. Huang, B. Zhai, S. Li, et al., Nano Energy 15 (2015) 244–255.
[98] K. Qin, L. Wang, N. Wang, J. Li, N. Zhao, C. Shi, et al., J. Mater. Chem. A 5 (2017) 18535–18541.
[99] L. Pei, Q. Jin, Z. Zhu, Q. Zhao, J. Liang, J. Chen, Nano Res. 8 (2015) 184–192.
[100] X. Xu, J. Liu, J. Liu, L. Ouyang, R. Hu, H. Wang, et al., Adv. Funct. Mater. 28 (2018) 1707573.
[101] X. Deng, S. Zhu, F. He, E. Liu, C. He, C. Shi, et al., Electrochim. Acta 283 (2018) 1269–1276.
[102] Y. Zhang, A. Wang, T. Zhang, Chem. Commun. 46 (2010) 862–864.
[103] X. Deng, S. Zhu, J. Li, L. Ma, F. He, E. Liu, et al., Nanoscale 9 (2017) 6478–6485.
[104] S. Zhu, J. Li, Q. Li, C. He, E. Liu, F. He, et al., Electrochim. Acta 212 (2016) 621–629.
[105] M. Liu, S. He, W. Chen, Nanoscale 6 (2014) 11769–11776.
[106] X.C. Dong, H. Xu, X.W. Wang, Y.X. Huang, M.B. Chan-Park, H. Zhang, et al., ACS Nano 6 (2012) 3206–3213.
[107] J. Sha, R.V. Salvatierra, P. Dong, Y. Li, S.K. Lee, T. Wang, et al., ACS Appl. Mater. Interfaces 9 (2017) 7376–7384.

[108] K. Qin, L. Wang, S. Wen, L. Diao, P. Liu, J. Li, et al., J. Mater. Chem. A 6 (2018) 8109–8119.
[109] J.W. Zhou, J. Qin, X. Zhang, C.S. Shi, E.Z. Liu, J.J. Li, et al., ACS Nano 9 (2015) 3837–3848.
[110] S. Zhu, K. Xu, S. Sui, J. Li, L. Ma, C. He, et al., J. Mater. Chem. A 5 (2017) 19175–19183.
[111] L. Wang, X. Li, T. Guo, X. Yan, B.K. Tay, Int. J. Hydrogen Energy 39 (2014) 7876–7884.
[112] K. Chi, Z. Zhang, Q. Lv, C. Xie, J. Xiao, F. Xiao, et al., ACS Appl. Mater. Interfaces 9 (2017) 6044–6053.
[113] H. Nishihara, T. Kyotani, Chem. Commun. 54 (2018) 5648–5673.
[114] X. Qiu, X. Yan, H. Pang, J. Wang, D. Sun, S. Wei, et al., Adv. Sci. 6 (2019) 1801103.
[115] Y.S. Wei, M. Zhang, M. Kitta, Z. Liu, S. Horike, Q. Xu, J. Am. Chem. Soc. 141 (2019) 7906–7916.
[116] B. Zhan, C. Liu, H. Chen, H. Shi, L. Wang, P. Chen, et al., Nanoscale 6 (2014) 7424–7429.
[117] C. He, S. Wu, N. Zhao, C. Shi, E. Liu, J. Li, ACS Nano 7 (2013) 4459–4469.
[118] F. Wen, H. Hou, J. Xiang, X. Zhang, Z. Su, S. Yuan, et al., Carbon 89 (2015) 372–377.
[119] C.G. Zhang, Z.W. Peng, J. Lin, Y. Zhu, G.D. Ruan, C.C. Hwang, et al., ACS Nano 7 (2013) 5151–5159.
[120] Y. Song, T. Liu, F. Qian, C. Zhu, B. Yao, E. Duoss, et al., J. Colloid Interface Sci. 509 (2017) 529–545.
[121] J. Liu, Y. Zhang, L. Zhang, F. Xie, A. Vasileff, S.Z. Qiao, Adv. Mater. 31 (2019) 1901261.
[122] C. Zeng, F. Xie, X. Yang, M. Jaroniec, L. Zhang, S.Z. Qiao, Angew. Chem. Int. Ed. 57 (2018) 8540–8544.
[123] J.Y. Hwang, S.T. Myung, Y.K. Sun, Chem. Soc. Rev. 46 (2017) 3529–3614.
[124] W. Liu, M.-S. Song, B. Kong, Y. Cui, Adv. Mater. 29 (2017) 1603436.
[125] X. Liu, J.-Q. Huang, Q. Zhang, L. Mai, Adv. Mater. 29 (2017) 1601759.
[126] Z.L. Xu, J.K. Kim, K. Kang, Nano Today 19 (2018) 84–107.
[127] D. Gu, W. Li, F. Wang, H. Bongard, B. Spliethoff, W. Schmidt, et al., Angew. Chem. Int. Ed. 54 (2015) 7060–7064.
[128] H. Ji, L. Zhang, M.T. Pettes, H. Li, S. Chen, L. Shi, et al., Nano Lett. 12 (2012) 2446–2451.
[129] H. Liu, W. Li, D. Shen, D. Zhao, G. Wang, J. Am. Chem. Soc. 137 (2015) 13161–13166.
[130] H.F. Wang, C. Tang, Q. Zhang, Nano Today 25 (2019) 27–37.
[131] W. Li, X. Sun, Y. Yu, Small Methods 1 (2017) 1600037.
[132] S. Feng, J. Song, C. Zhu, Q. Shi, D. Liu, J. Li, et al., ACS Appl. Mater. Interfaces 11 (2019) 5911–5918.
[133] G. Li, J. Sun, W. Hou, S. Jiang, Y. Huang, J. Geng, Nat. Commun. 7 (2016) 10601.
[134] Q. Yu, Y. Lu, R. Luo, X. Liu, K. Huo, J.K. Kim, et al.,Adv. Funct. Mater. 28 (2018), 1804520.
[135] C. Ye, Y. Jiao, H. Jin, A.D. Slattery, K. Davey, H. Wang, et al., Angew. Chem. Int. Ed. 57 (2018) 16703–16707.
[136] Y.Y. Wang, B.H. Hou, Q.L. Ning, W.L. Pang, X.H. Rui, M. Liu, et al., Nanotechnology 30 (2019) 214002.
[137] D. Wang, Z. Wang, Y. Li, K. Dong, J. Shao, S. Luo, et al., Appl. Surf. Sci. 464 (2019) 422–428.
[138] W. Li, S. Hu, X. Luo, Z. Li, X. Sun, M. Li, et al., Adv. Mater. 29 (2017) 1703311.
[139] F. Xie, L. Zhang, D. Su, M. Jaroniec, S.Z. Qiao, Adv. Mater. 29 (2017) 1700989.
[140] Y. Xu, W. Li, F. Zhang, X. Zhang, W. Zhang, C.S. Lee, et al., J. Mater. Chem. A 4 (2016) 3697–3703.
[141] X. Liu, J. Zai, B. Li, J. Zou, Z. Ma, X. Qian, J. Mater. Chem. A 4 (2016) 10552–10557.
[142] W. Luo, P.F. Zhang, X.P. Wang, Q.D. Li, Y.F. Dong, J.C. Hua, et al., J. Power Sources 304 (2016) 340–345.
[143] X. Zhao, H.E. Wang, R.C. Masse, J. Cao, J. Sui, J. Li, et al., J. Mater. Chem. A 5 (2017) 7394–7402.
[144] W.Y. Tsai, R.Y. Lin, S. Murali, L.L. Zhang, J.K. McDonough, R.S. Ruoff, et al., Nano Energy 2 (2013) 403–411.
[145] P. Simon, Y. Gogotsi, Nat. Mater. 7 (2008) 845–854.
[146] S. Zhu, J. Li, L. Ma, C. He, E. Liu, F. He, et al., Mater. Lett. 233 (2018) 294–297.
[147] F. Zhang, T.Y. Liu, M.Y. Li, M.H. Yu, Y. Luo, Y.X. Tong, et al., Nano Lett. 17 (2017) 3097–3104.
[148] M.J. Mostazo-López, R. Ruiz-Rosas, A. Castro-Muñiz, H. Nishihara, T. Kyotani, E. Morallon, et al., Carbon 129 (2018) 510–519.
[149] W. Li, F. Zhang, Y. Dou, Z. Wu, H. Liu, X. Qian, et al., Adv. Energy Mater. 1 (2011) 382–386.
[150] T. Lin, I.W. Chen, F. Liu, C. Yang, H. Bi, F. Xu, et al., Science 350 (2015) 1508–1513.
[151] J. Zhao, Y. Jiang, H. Fan, M. Liu, O. Zhuo, X. Wang, et al.,Adv. Mater. 29 (2017), 1604569.
[152] P. Jeżowski, O. Crosnier, E. Deunf, P. Poizot, F. Béguin, T. Brousse, Nat. Mater. 17 (2018) 167–173.
[153] J. Luo, W. Zhang, H. Yuan, C. Jin, L. Zhang, H. Huang, et al., ACS Nano 11 (2017) 2459–2469.
[154] H. Sun, J. Zhu, D. Baumann, L. Peng, Y. Xu, I. Shakir, et al., Nat. Rev. Mater. 4 (2018) 45–60.
[155] X. Cui, Y. Xu, L. Chen, M. Zhao, S. Yang, Y. Wang, Appl. Catal. B–Environ. 244 (2019) 957–964.
[156] V.R. Stamenkovic, D. Strmcnik, P.P. Lopes, N.M. Markovic, Nat. Mater. 16 (2017) 57–69.
[157] J. Ding, S. Ji, H. Wang, B.G. Pollet, R. Wang, ChemCatChem 11 (2019) 1026–1032.
[158] J. Ding, S. Ji, H. Wang, V. Linkov, H. Gai, F. Liu, et al., ACS Sustain. Chem. Eng. 7 (2019) 3974–3981.
[159] J. Zhang, Z. Zhao, Z. Xia, L. Dai, Nat. Nanotechnol. 10 (2015) 444–452.
[160] H. Liu, X. Liu, W. Li, X. Guo, Y. Wang, G. Wang, et al.,Adv. Energy Mater. 7 (2017), 1700283.
[161] J. Liu, N.P. Wickramaratne, S.Z. Qiao, M. Jaroniec, Nat. Mater. 14 (2015) 763–774.
[162] D.W. Kim, O.L. Li, N. Saito, Phys. Chem. Chem. Phys. 17 (2015) 407–413.
[163] N.R. Sahraie, U.I. Kramm, J. Steinberg, Y. Zhang, A. Thomas, T. Reier, et al., Nat. Commun. 6 (2015) 8618.
[164] K.N. Dinh, Q. Liang, C.F. Du, J. Zhao, A.I.Y. Tok, H. Mao, et al., Nano Today 25 (2019) 99–121.
[165] Y. Chen, R. Ma, Z. Zhou, G. Liu, Y. Zhou, Q. Liu, et al., Adv. Mater. Interfaces 2 (2015) 1500199.
[166] G.H. Moon, A. Bähr, H. Tüysüz, Chem. Mater. 30 (2018) 3779–3788.
[167] E. Luo, M. Xiao, J. Ge, C. Liu, W. Xing, J. Mater. Chem. A Mater. Energy Sustain. 5 (2017) 21709–21714.
[168] H.J. Qiu, P. Du, K. Hu, J. Gao, H. Li, P. Liu, et al., Adv. Mater. 31 (2019) 1900843.
[169] R. Zhao, Z. Liang, S. Gao, C. Yang, B. Zhu, J. Zhao, et al., Angew. Chem. Int. Ed. 58 (2019) 1975–1979.

Shan Zhu is a research assistant at Tianjin University. He obtained his bachelor degree and doctorate degree at Tianjin University. His research interests focus on carbon-based nanomaterials and energy storage applications.

Naiqin Zhao is a professor in the School of Materials Science and Engineering at Tianjin University. She obtained her B.S. and pH.D. from Tianjin University. She was a visiting scholar at Illinois Institute of Technology and the Hong Kong Polytechnic University; and a visiting professor at Tohoku University and Vanderbilt University. Her current research interests focus on the synthesis and characteristics of the carbon nanophase and their applications in energy materials and structural composites.

Jiajun Li is a professor in the School of Materials Science and Engineering at Tianjin University. He obtained his pH.D. from Swansea University, UK in 1995. His current research interests focus on nano materials and the behavior with the environmental interaction.

Xiaoyang Deng is a pH.D. student under the supervision of Prof. Jiajun Li and Prof. Naiqin Zhao in the School of Materials Science and Engineering at Tianjin University. He received his bachelor's degree from Qingdao University of Science and Technology in 2014. His current research focus on fabrication of MOF-derived carbon-based materials and their applications in supercapacitors and other energy storage devices.

Junwei Sha is a lecturer in the School of Materials Science and Engineering at Tianjin University. He obtained his bachelor's, master's, and doctor's degrees from Tianjin University, under the supervision of Prof. Naiqin Zhao. He was a visiting pH.D. student in Prof. James Tour's group in Department of Chemistry at Rice University. His current research interests focus on the development of carbon-based materials in energy storage and conversion, metal matrix composites, and 3D printing.

Chunnian He is a professor in the School of Materials Science and Engineering at Tianjin University. He obtained his bachelor's, master's, and doctor's degrees from Tianjin University. He is mainly engaged in the design, strengthening and toughening mechanism and application of metal matrix composites.